Andean Geology 41 (3): 558-588. September, 2014
doi: 10.5027/andgeoV41n3-a04

Andean Geology
formerly Revista Geológica de Chile
www.andeangeology.cl

The origin and emplacement of Domo Tinto, Guallatiri volcano, Northern Chile

Robert B. Watts[1], Jorge Clavero Ribes[2], R. Stephen J. Sparks[3]

[1] *Office of Disaster Management, Jimmit, Roseau, Commonwealth of Dominica.*
robbowatts@hotmail.com

[2] *Escuela de Geología, Universidad Mayor, Manuel Montt 367, Providencia, Santiago, Chile.*
jorge.clavero@umayor.cl

[3] *Department of Earth Sciences, University of Bristol, Wills Memorial Building, Queens Road, Bristol. BS8 1RJ. United Kingdom.*
steve.sparks@bristol.ac.uk

ABSTRACT. Guallatiri Volcano (18°25'S, 69°05'W) is a large edifice located on the Chilean Altiplano near the Bolivia/Chile border. This Pleistocene-Holocene construct, situated at the southern end of the Nevados de Quimsachata chain, is an andesitic/dacitic complex formed of early stage lava flows and later stage coulées and lava domes. Domo Tinto (5±3 ka, recent $^{40}Ar/^{39}Ar$ date) is a small dome located on the southern flanks of Guallatiri Volcano. It is composed of monotonous, crystal-rich andesite (~62% SiO_2) with predominant plagioclase, amphibole, biotite and rare clinopyroxene within a glassy groundmass containing plagioclase and subordinate amphibole microlites. Geochemical data indicate the Tinto lava is compositionally homogeneous. The occurrence of ovoid magmatic inclusions of basaltic andesite (<0.5% volume) and ubiquitous disequilibrium features in the mineral assemblage indicate that the magma chamber was perturbed by repeated intrusions of mafic magma. These events promoted magma-mingling, inclusion disaggregation and convective self-mixing before a critical recharge event triggered eruption and formation of the dome. Glacially eroded sections through Domo Tinto indicate that it was formed by the sequential extrusion of several hummocky lobes with a sub-horizontal base and a convex-upward upper surface. Each lobe exhibits a thin, basal zone of foliated lava and a thick interior of massive lava (up to ~20 m thick) and these lobes have piled atop each other to form an overall pancake morphology. The lack of any associated explosive material and collapse-scar features indicate the formation of Domo Tinto was relatively benign.

Keywords: Guallatiri, Geology, Low-dome, Hummock, Extrusion.

RESUMEN. Origen y emplazamiento del Domo Tinto, volcán Guallatiri, Norte de Chile. El volcán Guallatiri (18°25'S, 69°05'W) es un edificio volcánico ubicado en el Altiplano del norte de Chile, cercano a la frontera con Bolivia. Este volcán, construido en el Pleistoceno-Holoceno en el extremo sur de la cadena volcánica de los nevados de Quimsachata, corresponde a un complejo de composiciones predominantes andesítica y dacítica. En su primera etapa de formación, emitió esencialmente lavas y, en su segunda etapa, 'coulées' y lavas-domo. El Domo Tinto (5±3 ka, datación $^{40}Ar/^{39}Ar$) es un domo de pequeño volumen ubicado en el flanco sur del volcán Guallatiri. Está compuesto por andesitas ricas en cristales (~62% SiO_2) con fenocristales de plagioclasa, anfíbola, biotita y escaso clinopiroxeno inmersos en una masa fundamental vítrea con microlitos de plagioclasa y menor proporción de anfíbola. Los datos geoquímicos indican que la composición del magma que dio origen al Domo Tinto es composicionalmente homogénea. La ocurrencia de enclaves magmáticos ovoidales de composición andesítico-basáltica (<0.5% volumen) y la ubicuidad de texturas de desequilibrio mineral indican que la cámara magmática fue perturbada por numerosas intrusiones de magma máfico. Estas intrusiones promovieron procesos de mezcla de magma, desagregación de inclusiones y automezcla convectiva previo a la recarga crítica que finalmente gatilló la erupción que generó el Domo Tinto. Secciones del Domo Tinto afectadas por erosión glacial permiten señalar que él se formó por la extrusión secuencial de varios lóbulos con morfología rugosa de cerrillos, con base subhorizontal y un techo superior convexo hacia arriba. Cada lóbulo exhibe una delgada zona basal foliada y una potente zona interior formada por lava maciza con diaclasamiento irregular. Los lóbulos se apilaron uno encima de otro y formaron una morfología singular tipo 'panqueque' con distintivos cerrillos lineales en la superficie superior. La ausencia de depósitos piroclásticos y de escarpes de colapso asociados indican que la formación del Domo Tinto fue relativamente tranquila. Este tipo de domos bajos con morfología de cerrillos puede ser una fase común tardía de erupción de flanco en estratovolcanes de los Andes centrales.

Palabras clave: Guallatiri, Geología, Tipo-torta, Cerrillo, Extrusión.

1. Introduction

An important aspect of effusive volcanism is to understand the dynamics of magma ascent and emplacement and to predict the consequent eruptive hazards for magmas that range the entire compositional spectrum. Until recently, the understanding of basaltic lava emplacement had been more advanced with the near-continuous effusive activity on Hawaii and their relative quiescent outpourings allowing for close observation (*e.g.*, Hon *et al.*, 1994). Understanding of silicic lavas have included studies of structures using textural and morphological observations to detail their emplacement (*e.g.,* Fink, 1983). Remarkable strides have also been achieved through the intense monitoring at eruptions of intermediate composition lavas at Mount St. Helens in 1980-86 and 2004-06 (*e.g.,* Swanson *et al.,* 1987; Vallance *et al.,* 2008; Cashman *et al*., 2008), Mount Unzen in 1991-95 (*e.g.,* Nakada *et al.,* 1999; Browne *et al.*, 2006), Mount Redoubt in 2009 (*e.g.,* Bull *et al.*, 2013) and the on-going Soufrière Hills eruption (*e.g.,* Sparks and Young, 2002). In the latter example, the repeated emplacement of asymmetric lobes of crystal-rich andesitic lava was observed to occur sequentially in a directed manner away from a central conduit (Watts *et al.*, 2002). Such activity directed large-scale dome collapse pyroclastic flows down every flank of the volcano and devastated the landscape in all directions around the main edifice. Despite these advances, it has always been too hazardous to attempt detailed ground inspections of the active domes such that structural and textural studies across an individual dome-lobe were not possible. As a result, detailed knowledge regarding their internal structure is still very limited. This study is partly an attempt to address this problem through the investigation of exposures of a young, inactive dome whose interior has been exposed by recent glacial advances.

Domo Tinto is a small structure on the flanks of Guallatiri Volcano in northern Chile (18°25'S, 69°05'W) located in the north-east corner of Region XV (Fig. 1). This dome is similar in composition and textural character to the Soufrière Hills lava. A petrological study of this lava is presented, along with field observations across the dome to provide an emplacement history and petrogenetic model for Domo Tinto. The formation of Domo Tinto is placed in the context of the geological evolution of Guallatiri Volcano.

2. Geologic Setting and Geology of Guallatiri Volcano

The basement of Guallatiri Volcano is mainly formed by volcaniclastic and sedimentary units, which range in age between Upper Oligocene and Pleistocene (Fig. 2). The oldest basement units are located to the north, west and south of the volcano, and consist mainly of welded rhyolitic ignimbrites, epiclastic sandstones and laharic breccias of the Upper Oligocene to Lower Miocene Lupica Formation (Montecinos, 1963; García *et al.*, 2004). This volcanic sequence is moderately to strongly folded and locally affected by reverse faults (Muñoz and Charrier, 1996). During the Upper Miocene to Pleistocene, to the west of the volcano a lacustrine basin was developed; the Lauca Basin (Kött *et al.*, 1995). Inter-bedded within these lacustrine sediments there is an extensive rhyolitic ignimbrite, the 2.7 Ma Lauca Ignimbrite (Wörner *et al.*, 2000; García *et al.*, 2004) equivalent to the Pérez Ignimbrite in Bolivia. This ignimbrite was probably sourced from a sub-circular structure around Sajama volcano in western Bolivia, although detailed studies need to be carried out to confirm this hypothesis. In the final evolutionary stages of this basin, a large glacial field developed, partially covering it with moraines, fluvioglacial and lacustrine deposits. Contemporaneous with these glacial episodes, the Quimsachata volcanic chain, to which Guallatiri Volcano belongs, started to form. Glacial deposits are therefore widespread around the volcano, partially forming its base and inter-bedded with lava flows, domes and pyroclastic deposits particularly on its southern flank.

Guallatiri Volcano (18°25'S, 69°05'W) is located at the south-western end of a ~50 km long volcanic chain, elongated in NS to NE-SW direction, on the border between Bolivia and Chile (de Silva and Francis, 1991). This chain is known as the Nevados de Quimsachatas and is formed by four eruptive centres, from north to south: Humarata, Acotango, Capurata and Guallatiri volcanoes (González, 1995; García *et al.,* 2004; Fig. 3a). The main focus of eruptive activity has migrated from north to south during the Quaternary. Humarata and Acotango are both Early Pleistocene volcanoes that have been deeply eroded by glacial activity (Fig. 3b). The erosion has left their cores partially exposed, especially on their western flanks, showing important zones affected by hydrothermal alteration. The

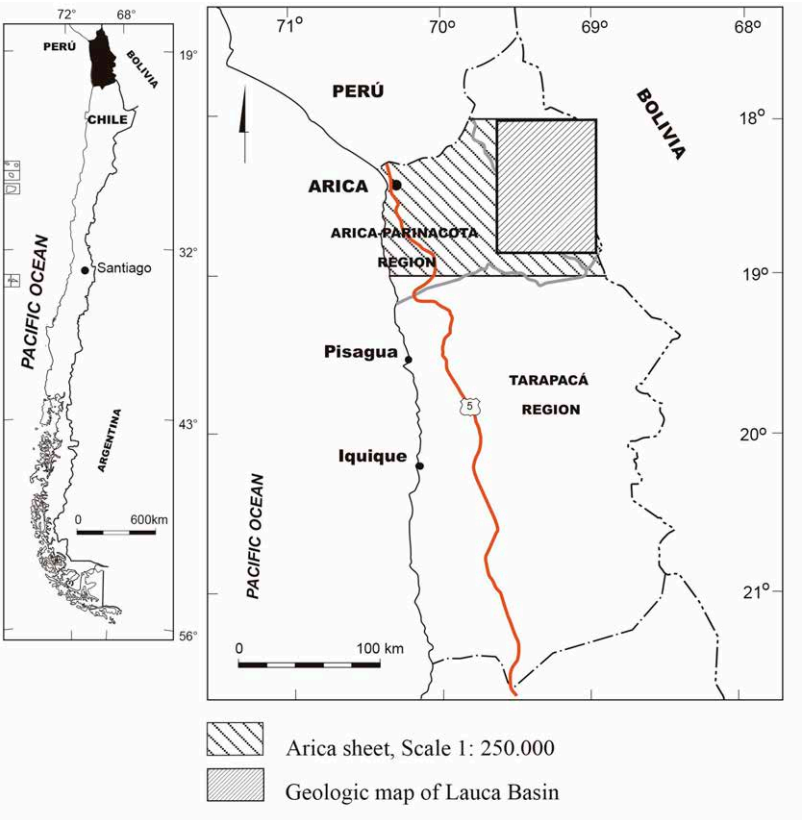

FIG. 1. Location map of Tarapaca Region XV in northern Chile. Rectangle indicates location of the Lauca Basin within which Guallatiri Volcano is found. Inset map shows the position of Region XV in Chile.

southernmost centres, Capurata and Guallatiri, have better preserved primary morphologies, both of the centres themselves and their products, although zones affected by hydrothermal alteration mainly associated with fumarolic activity are also present in both volcanoes.

Guallatiri Volcano (altitude 6,063 m) has a vigorous fumarole field near its ice-capped summit. Andesitic lavas spill away from the main edifice in all directions whilst the outer flanks are marked by andesitic and dacitic domes of a variable size, including Domo Tinto (Figs. 4 and 5). The evolution of Guallatiri Volcano can be divided into two stages, from a volcano predominantly formed of thick andesitic to dacitic lava flows (Stage I) to a dome complex with associated pyroclastic deposits in its second stage (Stage II). Lava flows from Stage I have relatively well preserved primary morphologies, such as levées and flow ridges slightly smoothed by glacial erosion (Fig. 4). The flows are up to 7 km long and 100 m high and partially covered by morainic breccias. Stage II domes developed on top of Stage I flows and have very well-preserved primary morphologies although some flank domes (including Domo Tinto) have been partially dissected by Late Pleistocene-Holocene glaciers. The domes have sub-circular shapes with basal diameters up to 1,000 m and up to 200 m high. According to their erosive features and two whole-rock K-Ar dates, García *et al.*, (2004) suggested that Stage I flows were erupted during the Middle Pleistocene, while Stage II domes formed during the Late Pleistocene-Holocene. Guallatiri Volcano has permanent fumarolic activity (de Silva and Francis, 1991; Simkin and Siebert, 1994; González, 1995), at least on the upper part of two of its flanks (to the west and south) and has produced a series of small explosive eruptions in historic times (Simkin and Siebert, 1994; Newhall and Melson, 1983). It is also the southernmost volcano in the Central Andes with a permanent ice cap.

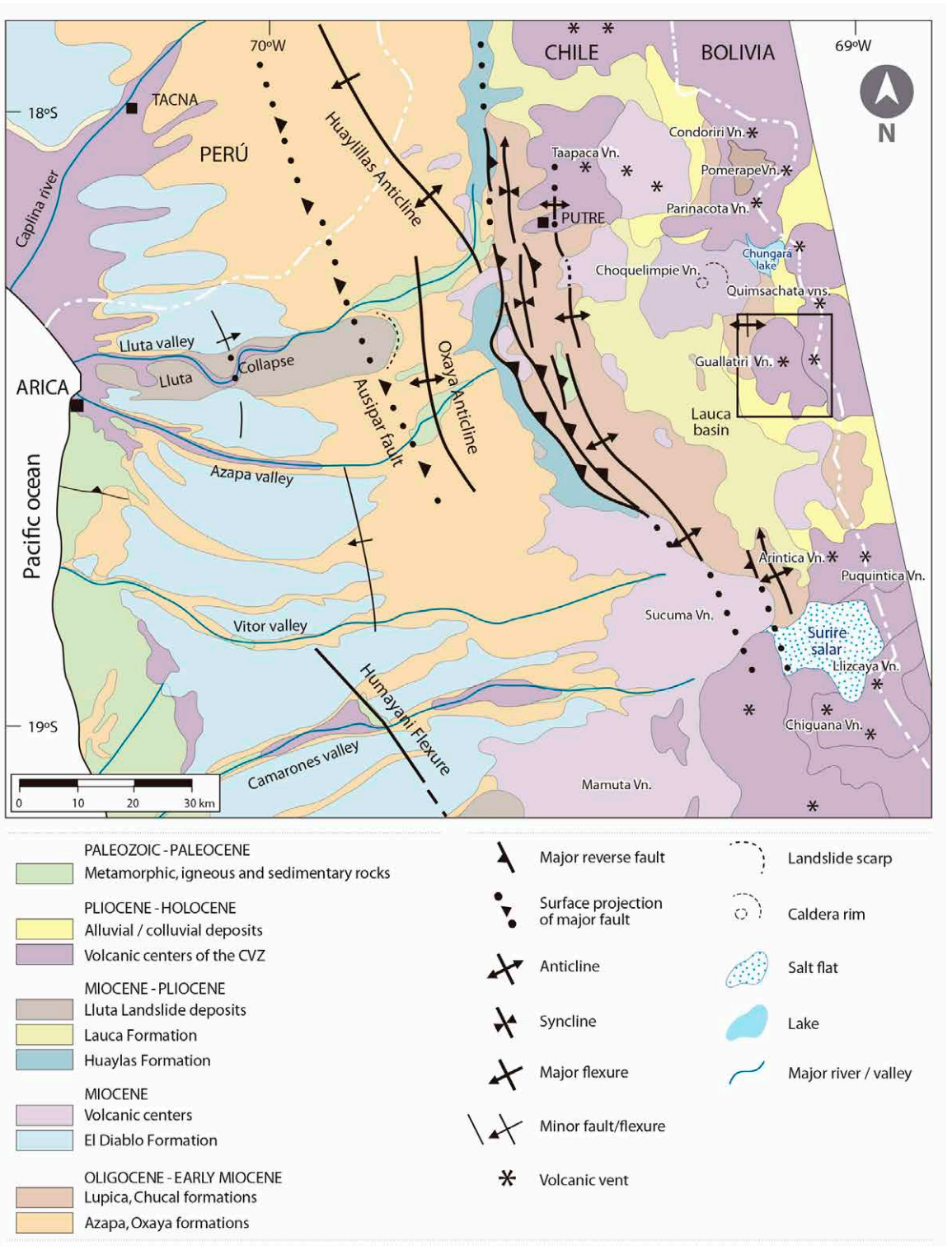

FIG. 2. Regional geologic map of the Chilean Altiplano in Region XV, with the Lauca Basin area near to the border with Bolivia (modified from Charrier *et al.*, 2013) and Guallatiri Volcano highlighted in the black square.

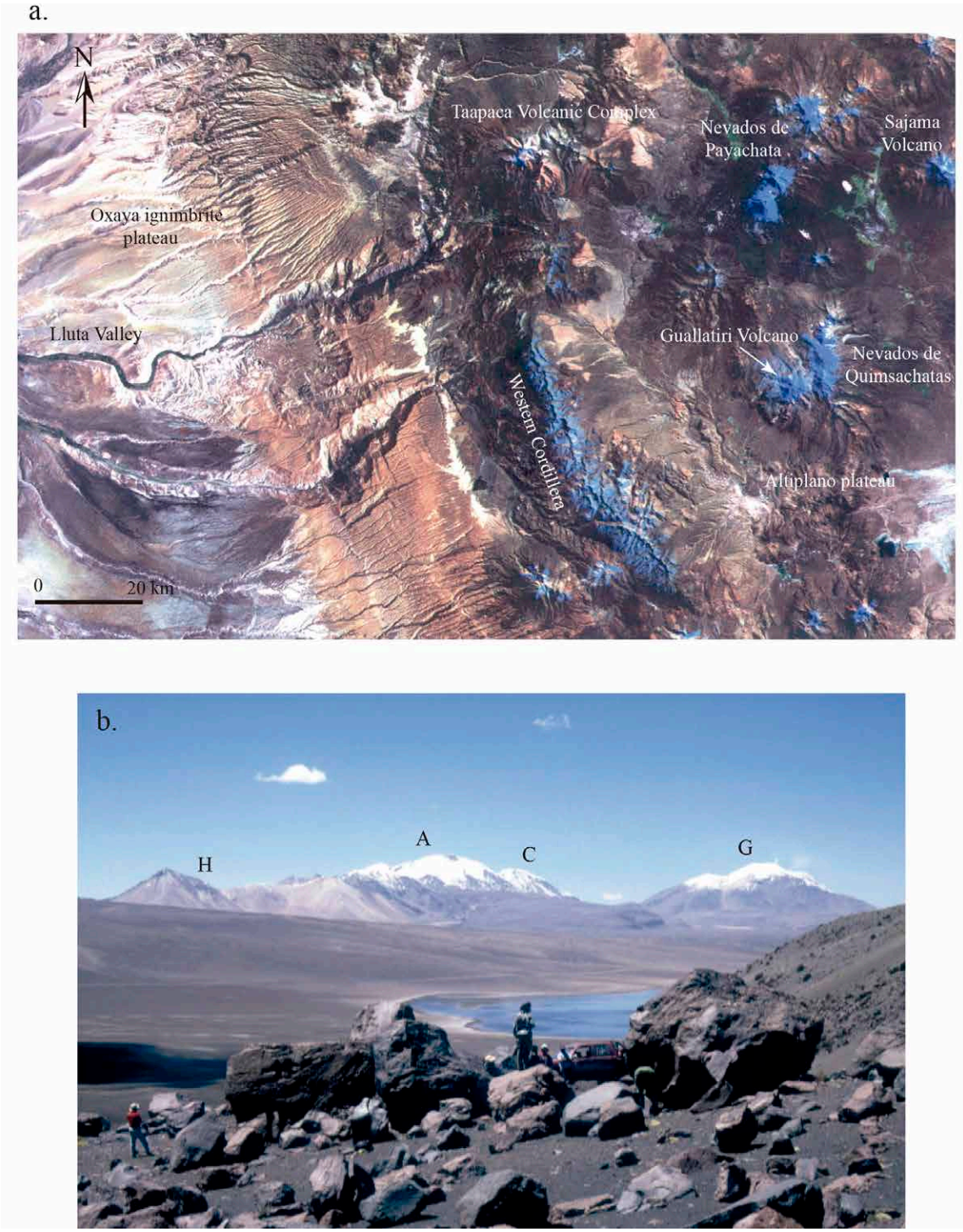

FIG. 3. **a.** Landsat TM Image of North Chilean Altiplanic region (Bands 7, 4 and 1; blue areas are snow-capped summits). The Lauca Basin area is seen to the right; **b.** View looking south at the Nevados De Quimsachatas highlighting their more eroded appearance with distance from the southernmost part of Guallatiri Volcano; **G:** showing summit fumarole fields. Other peaks are: **H:** Volcans Humarata; **A:** Acotango; **C:** Capurata.

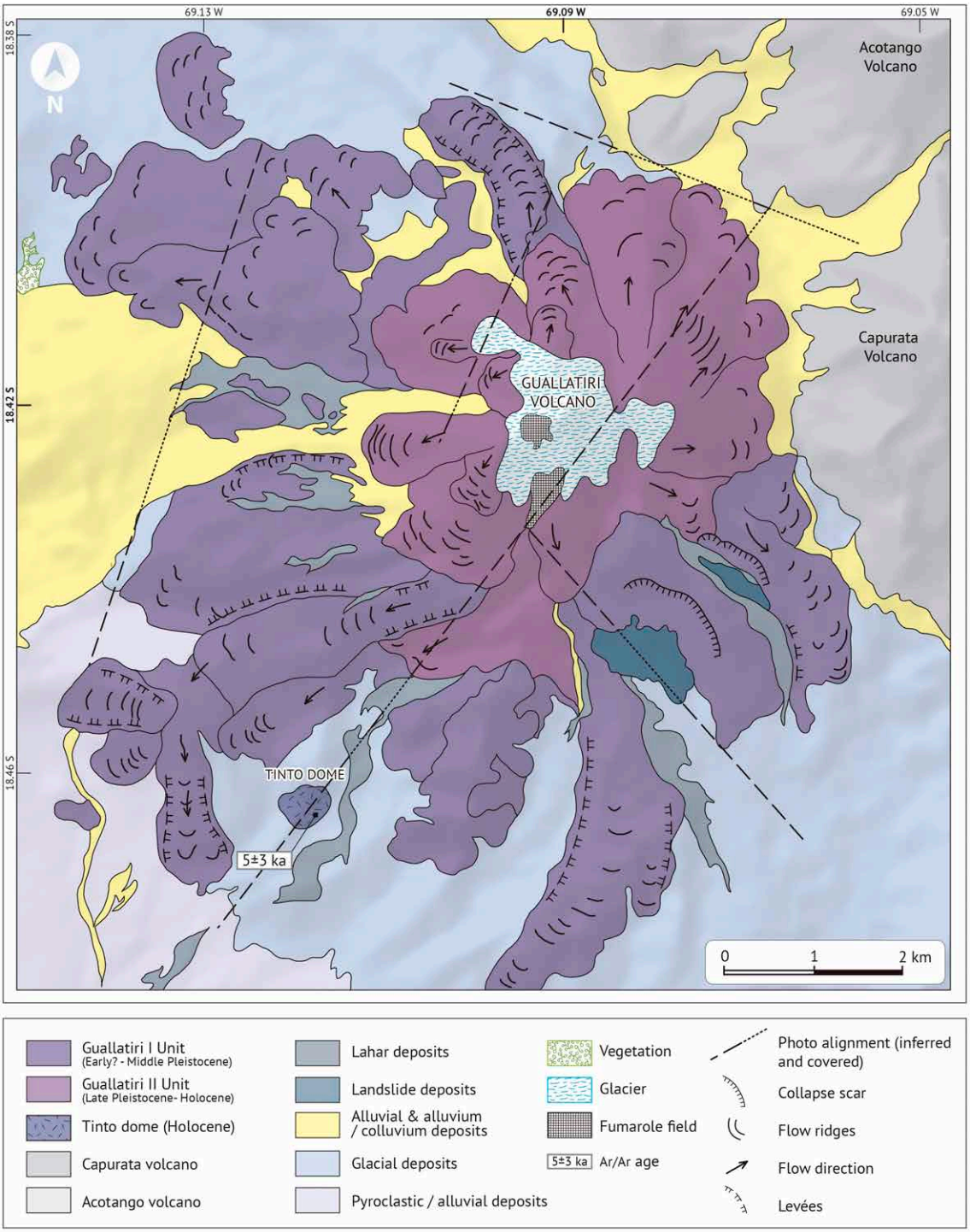

FIG. 4. Geologic map of the Guallatiri Volcano edifice.

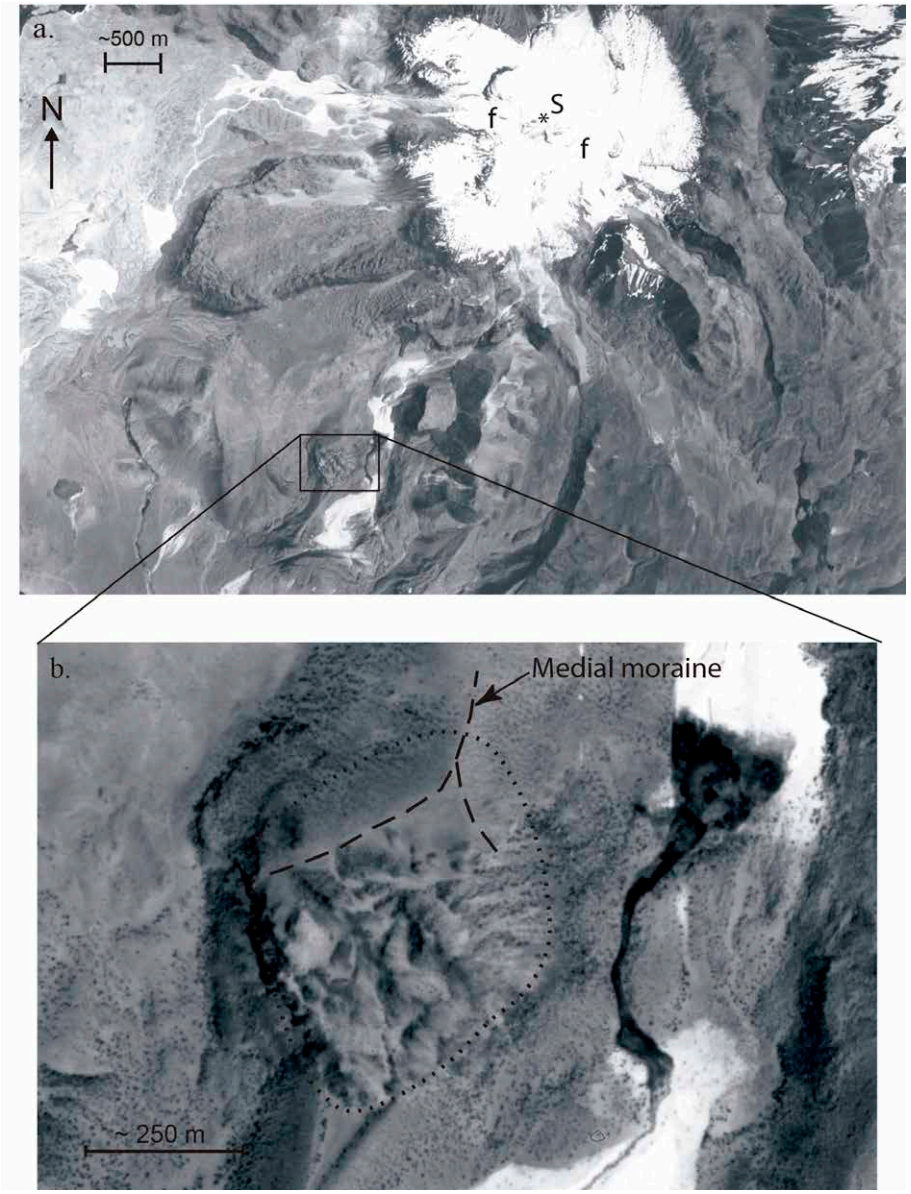

FIG. 5. **a.** Aerial photograph of Guallatiri Volcano showing the numerous andesitic to dacitic flows and domes around the snow-capped main edifice. **S** marks the summit and **f** is location of a fumarole field. Domo Tinto is shown in the enclosed box on the SW flanks; **b.** Close-up of Domo Tinto, ~500 m in diameter, where approximate outline is marked by a dotted line. Note the contrast between the central and southern sectors of the summit (marked by bright, elongate features and shaded areas) and the northern summit area (structure-less and monotonous shading).

3. The Geology of Domo Tinto

The structure forming the main focus of this study is Domo Tinto, a relatively small feature ~500 m in diameter and ~80-100 m high nestled on the outer SSW flanks of the Guallatiri Volcano (Figs. 5a, 6b). Domo Tinto is one of the smallest Stage II domes, having a total volume of ~2.0×10^7 m^3 and located on a ridge between two large valleys. Here we present a new date that yielded 5±3 ka using $^{40}Ar/^{39}Ar$ geochronology. Both the steep eastern and western flanks of the dome have been extensively

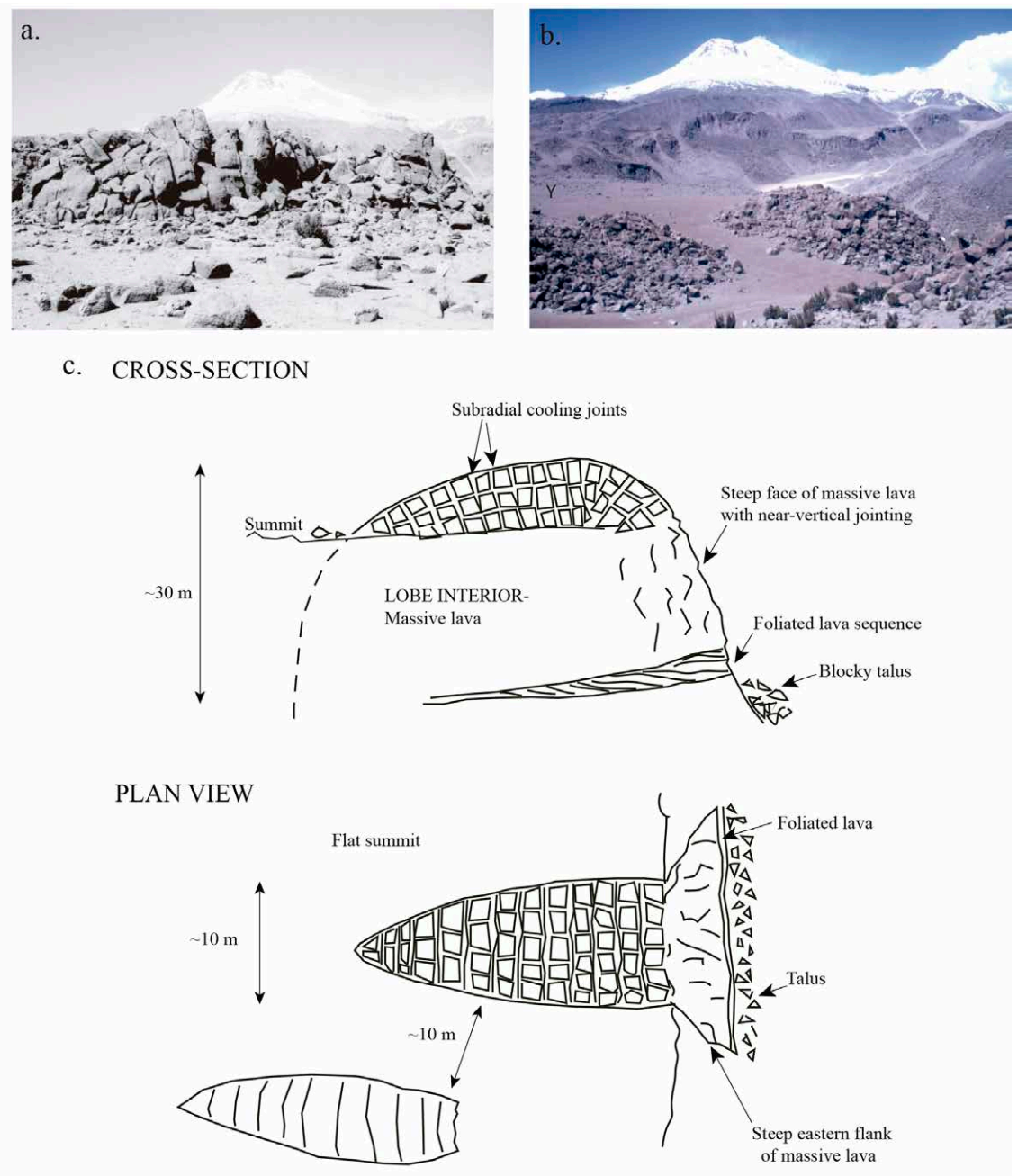

FIG. 6. **a.** View of typical hummock on central summit area ~50 m long, 5 m high and 10 m wide. Note the smooth outline of overall structure and sub-radial jointing forming mosaic-effect where blocks have remained in place despite periglacial activity. The right-hand side of the structure is more chaotic where blocks have tumbled away from their original position. Main edifice in background; **b.** View looking north from summit of the dome. Note the contrast in topography at point **Y** on the dome summit where it is relatively flat, devoid of structures and littered with loose blocks of a moraine deposit. Main edifice in background; **c.** Cross-section and plan-view showing the morphological features of a singe hummock observed on eastern flank of the dome highlighting the sub-radial jointing that grades down into a broad face of massive lava underlain by a thin zone of sub-horizontal foliated lava. At the summit, each hummock is separated from adjacent hummocks by a flat area of small rubbly scree.

scoured by valley glaciers and the blocky talus characteristic of crystal-rich domes has been almost entirely removed by this glacial activity. The northern summit area has a relatively featureless appearance as it is covered by a blanket of morainic debris from this glaciation. However, the overall summit area is not covered by moraine and original emplacement features of the dome are apparent.

Domo Tinto covers an area of $2x10^5$ m^2 and a moderate Aspect Ratio of 5.5 (where Aspect Ratio, as defined by Walker (1973), is the diameter of a circle of equivalent area to the footprint of the dome divided by its average thickness). It has a pancake torta-like form, typical of many Andean domes (*e.g.,* Cerro Chascon, SW Bolivia; Watts *et al.,* 1999), with an apparent hummocky, upper surface (Fig. 6a) that is another characteristic feature of many crystal-rich domes. In the classification of Blake (1990), this dome would be considered a 'low-dome' with its roughly circular shape. Overall, Domo Tinto is composed of a monotonous, leucocratic, porphyritic lava (av. 37 vol.% phenocrysts; Table 1) of andesitic composition (av. 61.75% SiO_2). There is a small proportion (~0.5 vol.%) of ovoid mafic inclusions (~55% SiO_2).

Elongate rounded hummocks, slightly degraded by periglacial and glacial activity, are the most prominent feature on the summit and the upper third sector around the periphery of the dome. The hummocks vary in size from 5-50 m wide and 10-100 m long; a typical example being 3 m high, 20 m long and 10 m wide (Fig. 6c). Generally, they exhibit an overall smooth outline, often lenticular in plan view akin to the humpback of a whale, with the long axes of the lenticular structures crudely aligned in the east-west direction. These hummocky structures are ubiquitously broken up by a series of sub-radial cooling fractures. In some cases, the fracture-bound lava blocks remain in place despite the fracturing, thus a mosaic-type effect is common to the structure. In many other cases, the fracturing destabilizes the hummocks and lava blocks fall away forming a more haphazard pile of curvilinear blocks (Fig. 6a). A notable feature of the lava forming the hummock blocks is its relatively high vesicularity and lower density (1.78 g/cm^3 at the summit) in contrast to the lower parts of the dome (av. dome sample is 2.35 g/cm^3).

The central and southern summit areas exhibit many examples of these hummocks that are separated by sandy trails of loose crystals tens-of-metres wide. In stark contrast, the northern half of the summit area is devoid of hummocks with a relatively smooth, flat topography littered with random blocks of a denser, grey rock (up to 1 m in diameter). This sector of the summit area is towards the summit of Guallatiri Volcano and interpreted to have been covered by ice at the sides of a valley glacier. As a result, the original lava hummocks have either been plucked away or buried by morainic debris containing gravel and including andesitic lava blocks. At the eastern edge of the summit area, there is a distinct boundary between the two contrasting topographies. On the western edge, however, relict examples of hummocks are observed and a gradual transition from original hummocks to the flat topography of the northern sector is evident.

At the western edge of the dome, a steep south-western face has been carved by a valley glacier and exposes the dome interior. Prominent features include: **(i)** thick zones of massive lava (10-20 m thick) with sub-vertical fractures; **(ii)** thin horizontal zones showing well-developed, sub-horizontal flow laminations; and **(iii)** convex-upward dome-like contacts often on top of the massive zones (Fig. 7). The loose, blocky character of the hummocks at the summit grades down into underlying massive lava which displays extensive linear and curved fractures most likely formed by rapid cooling during extrusion (Fig. 7).

Despite the basal zone of the western flanks being hidden by talus, and the uppermost part of the section being inaccessible, systematic sampling across the lower to mid-section of this exposure was achieved. The most detailed sequence of textural and structural features was determined across a ~30 m high near-vertical face with a section along a prominent ledge in the lowermost part of the accessible western face (Fig. 8a). A distinct 3 m-thick zone of alternating massive and foliated lava was evident along this ledge (Figs 8b, 8c) at the base of a ~30 m thick sequence of massive lava. At the lower part of this layered sequence, the foliated lava (varying from 15-65 cm thick) was composed of a series of thin undulating layers (1 to 3 cm thick) with a banded appearance. The layering consisted of orange bands with prominent vesicles and dark grey bands with a more glassy appearance. This variation promoted differential weathering between the two bands. The phenocrysts in these layers showed a

TABLE 1. MODAL COUNT ANALYSES OF DOMO TINTO LAVAS.

Sample No.	TD01	TD03	TD04	TD05	TD06	TD07	TD08	TD10	TD14
	Mafic Incl.	Foliated layer	Massive lava	Foliated layer	Massive lava	Foliated layer	Massive lava	Hummock	N. summit
Phenocrysts (%)	10	38	33.6	35.6	40	39	41	28.6	46.8
Groundmass/Glass (%)	90	62	66.4	64.4	60	61	59	71.3	53.2
Phenocrysts									
Plagioclase	-	22.7	20.6	19.2	26	27.1	27.6	13.9	27.3
Plagioclase (altered)	5.1	-	-	-	-	-	-	-	-
Amphibole	0.7	3.8	2.4	2.1	2.8	0.4	1.9	8.25	14.8
Amphibole (altered)	-	10.4	7.8	11.9	8.9	9	8.2	0.5	1.1
Biotite	-	-	-	-	-	-	-	-	-
Biotite (altered)	2.2	0.1	1.7	0.9	1.1	1.2	1.4	1.25	0.2
Pyroxene	-	0.1	0.1	0.6	0.3	-	T	-	0.2
Opaques	1.6	0.9	1.1	0.9	0.9	1.3	1.9	0.9	3.2
Groundmass									
Amphibole	28	-	-	-	-	-	-	-	-
Plagioclase	58.2	-	-	-	-	-	-	-	-
Vesicles	4.2	-	-	-	-	-	-	-	-

* All data are volume percent on the basis of 1,600 points counted.

T - Trace amount present.

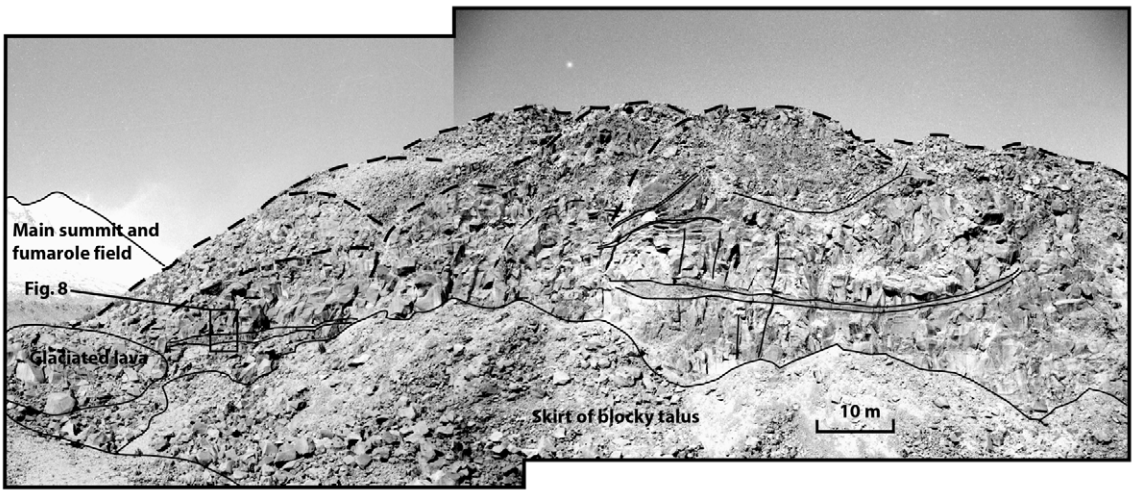

FIG. 7. Mosaic of photographs showing the exposed interior of the south-western flank (~80 m high) of Domo Tinto. The closely spaced solid lines represent thin zones of variably textured and foliated rock outlined in figure 8 while dashed lines show the upper boundary of thicker zones of massive lava. A crude pattern of individual sheets of lava with a relatively flat base and undulating upper surface can be discerned suggesting a stack of overlapping lava sheets. Near-vertical lines represent joints.

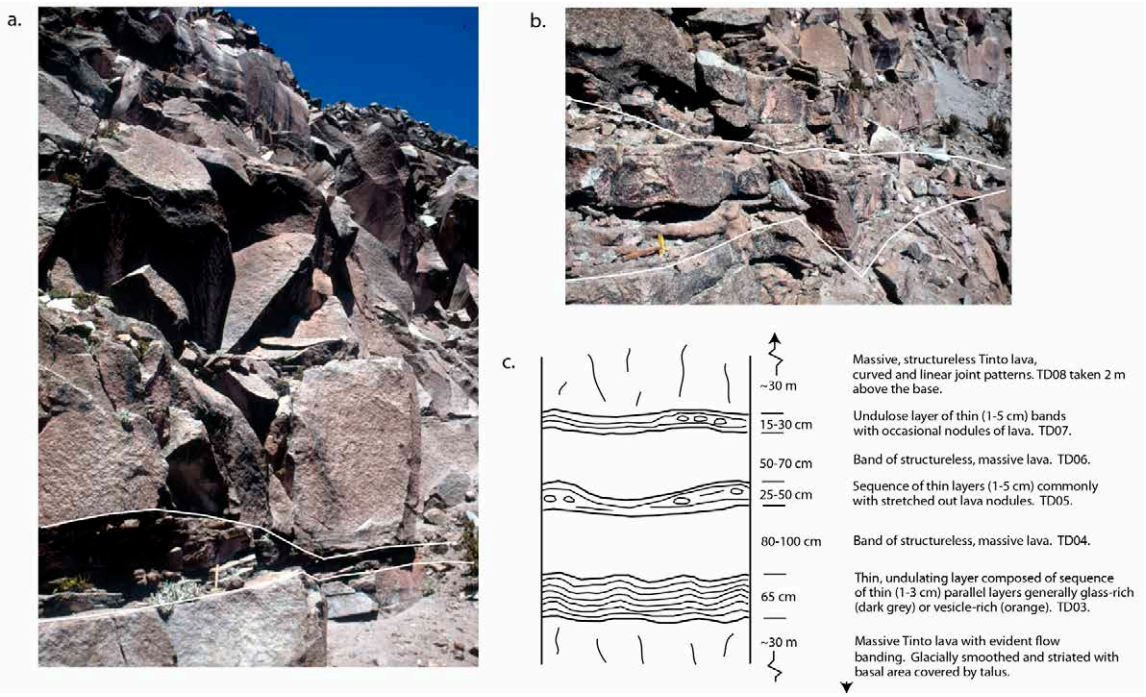

FIG. 8. **a.** Close-up view of section A shown in figure 7. This view highlights the thick zone of massive lava overlying a thin, undulose sequence at its base. Hammer is 30 cm long; **b.** Close-up of layered sequence consisting of thin bands of massive lava and weathered-out foliated layers with lava nodules. Hammer is 30 cm long; **c.** Stratigraphic column for layered sequence seen in **b**.

crude alignment with their long axes parallel to the layering, although no examples of fragmented crystals were observed within the layers. The entire layered zone exhibited a wavy, undulating upper and lower surface with the internal foliation mimicking these undulations. One prominent layer could be traced along the ledge for ~120 m before pinching out while other examples near the same horizon would pinch out after 5 to10 m.

The layers of massive lava separating the thinner layered zones were generally structureless and ranged in thicknesses of ~50 to 100 cm. Between these zones of massive lava were thinner bands of the undulating foliated lava that commonly contained boudinaged lava nodules (~5 to 10 cm wide) within some layers. At the top of the section, a thicker sequence of massive lava (up to ~30 m) graded up to the hummocky summit. This massive lava had distinctive curved jointing that eventually merged into the hummocks of loose blocks near the summit. A distant view of the entire south-western flank shows a sequence of similar structures stacked up on top of each other (Fig. 7).

4. Petrology of Domo Tinto

4.1. Methods

Standard thickness polished thin-sections for a selected number of samples were prepared and examined using a petrographic microscope. Mineral chemistry was analyzed on a Cameca Camebax Microprobe (housed at the Department of Earth Sciences, University of Bristol, U.K.) with SamX software and PAP correction for crystal phases using 15 kV accelerating voltage and 25 nA beam current. Modal analyses of phenocryst phases were determined on 10 samples by point counting. In the following descriptions, the crystal grain-size is divided into phenocrysts (>300 μm in diameter), micro-phenocrysts (between 300 to 100 μm) and microlites (<100 μm).

4.2. Tinto Lava samples

Generally, the dome-lava is porphyritic (25 to 48 vol.% phenocrysts) with an average 37 vol.% phenocrysts (Table 1). The predominant phenocrysts range from plagioclase > amphibole > biotite > pyroxene and these sit within a microlite-rich groundmass of silicic glass containing plagioclase microlites and subordinate amphibole microlites. The proportion of microlites within the groundmass varies from 30 to 50%. Dome samples analyzed include one from the centre of a massive lobe (#TD08), a foliated lava layer (#TD05) and a thin, massive layer (#TD04), both from the basal foliated sequence along with a vesicular block taken from a summit hummock (#TD10). Detailed probe analyses of each sample highlighted their similar nature and are thus described together.

Seriate-textured plagioclase (29 to 41 vol.%) is the most abundant phenocryst phase (Fig. 9) spanning a wide range of sizes (between 7 mm diameter to <100 μm microlites). The euhedral/subhedral plagioclase phenocrysts are generally andesine, yet wide-ranging in composition (An_{31}-An_{58}) with a distinctly bimodal nature (Fig. 9; Table 2). Ubiquitous examples of reversely-zoned phenocrysts with well-developed reaction rims and characteristic sieve-texture are present (Figs. 10a and b). Plagioclase phenocrysts also contain inclusions of brown glass and small prismatic crystals of apatite (colourless with a slight green tinge) and rare amphibole. Plagioclase with reaction rims are both normally and reversely zoned with substantial differences in anorthite content from core to rim (Fig. 11). A series of core-to-rim transects across phenocrysts show an oscillating Ab/An content although a broad trend passing from an Ab-rich core through to more calcic-rich zones and returning to a relatively Ab-rich rim was commonly recorded.

Plagioclase microphenocryst compositions are bimodal in character with modes at An_{54} and An_{35} (Fig. 9). Plagioclase microlites are commonly flow-aligned and distorted around phenocrysts and range from An_{17}-An_{58} but cluster around An_{54}. They are more calcic than the phenocryst population and similar to the microphenocrysts of the mafic inclusion (Fig. 9).

Amphibole is the most abundant ferromagnesian mineral (~10 vol.%) and ranges in size between 5 mm to < 100 μm (Tables 1 and 3). Amphibole phenocrysts are generally euhedral whilst microphenocrysts are more prismatic. The most revealing aspect of the amphibole is the range of alteration textures exhibited in the dataset. Commonly, amphibole is completely pseudomorphed by opacite composed of extremely fine-grained Fe-Ti oxide minerals. This opacite texture has been noted before

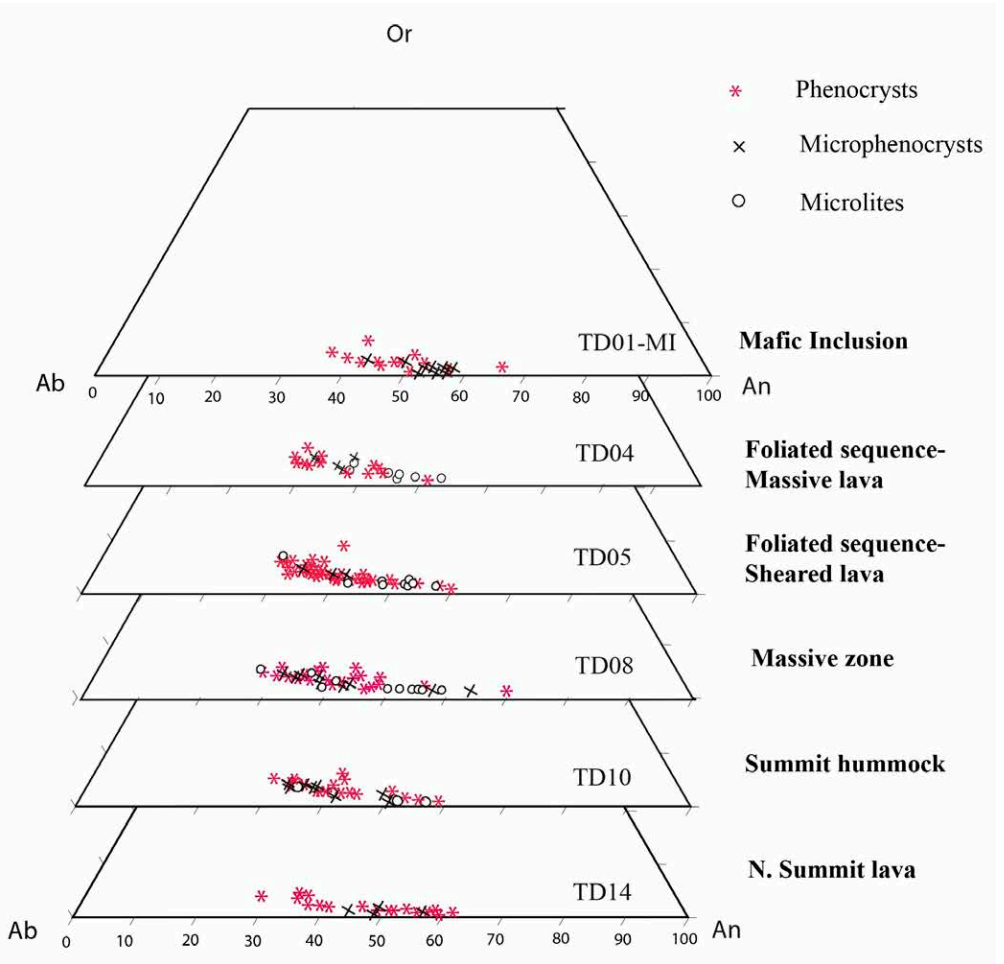

FIG. 9. Ternary diagrams showing the compositions of plagioclase crystals in all samples of the Domo Tinto dataset.

(*e.g.,* García and Jacobson, 1979) and has been described in other dome lavas (*e.g.,* Murphy *et al.*, 2000). In the latter, the authors distinguished between 3 types of amphibole alteration as Type 1 (forming a thin reaction rim), Type 2 (a coarse reaction rim) and Type 3 (complete alteration). This classification system is used here for the Guallatiri dataset. The coarser Type 2 rims with assemblages of coarse anhydrous crystals (up to 30 μm wide) have been described in Montserrat dome lavas and these are attributed to depressurisation during slow ascent in the conduit (Devine *et al.*, 1998). Such coarse rims are not observed in the Tinto lavas suggesting that all of the lava had ascended to the surface at a relatively fast rate. Phenocrysts of amphibole (between 300 to 1,000 μm) exhibit a thin reaction rim (between 10-30 μm wide) of micron-size crystals of Fe-Ti oxide and plagioclase. Microphenocrysts of amphibole predominantly exhibit coarser rims (between 30-60 μm wide) of similar re-crystallisation texture whilst amphibole microlites are almost completely pseudomorphed by opacitic alteration. These textures are interpreted as oxidation and dehydrogenation features developed following emplacement of the dome lava. Extensive 'stewing' of this lava during endogenous growth by migrating fluids gradually deteriorated the amphibole crystals up to the point of complete alteration.

Amphibole is mostly calcic edenite (from Leake *et al.,* 1997) with a few examples of pargasite and magnesiohastingsite (Fig. 12). Some magnesiohastingsite micro-phenocrysts are similar to amphiboles found in the mafic inclusions. Phenocrysts show partial alteration with corroded margins and microlites

TABLE 2. REPRESENTATIVE MICROPROBE ANALYSES OF PLAGIOCLASE CRYSTALS IN THE TINTO LAVAS (TL) AND MAFIC INCLUSIONS (MI).

Sample	GA TD08	GA TD08	GA TD08	GA TD10	GA TD10	GA TD08	GA TD08	GA TD10	GA TD10	GA TD08	GA TD08	GA TD08	MI TD01-MI	MI TD01-MI	MI TD01-MI	MI TD01-MI	MI TD01-MI
Type	Ph-C	Ph-C	Ph-C	PH-C	PH-R	MP-C	MP-C	MP	MP	MIC	MIC	MIC	PH-C	Ph-R	MIC	MIC	MIC
SiO_2	59.160	58.220	59.160	59.470	62.860	53.140	59.16	59.720	59.830	55.730	52.62	53.6	59.230	55.010	54.610	55.790	54.490
TiO_2	0.000	0.000	0.030	0.070	0.020	0.030	0.03	0.000	0.010	0.050	0.02	0.06	0.000	0.010	0.020	0.030	0.040
Al_2O_3	24.900	25.770	25.260	24.980	23.970	28.390	25.26	24.910	24.260	26.830	28.46	28.04	25.820	27.410	27.890	27.490	27.850
Fe_2O_3	0.340	0.170	0.000	0.390	0.350	0.580	0	0.270	0.320	0.790	0.79	0.46	0.270	0.740	0.470	0.530	0.540
MgO	0.000	0.020	0.000	0.140	0.150	0.070	0	0.020	0.020	0.020	0.06	0.05	0.010	0.020	0.020	0.030	0.020
CaO	7.350	8.200	7.320	7.700	6.050	11.530	7.32	8.160	6.680	10.020	12.02	11.31	7.730	10.460	10.790	10.140	11.020
Na_2O	7.020	6.460	6.970	6.550	7.260	4.750	6.97	6.310	7.310	5.570	4.61	4.89	6.350	5.580	5.440	5.720	5.450
K_2O	0.790	0.550	0.710	0.690	1.000	0.310	0.71	0.470	0.860	0.440	0.33	0.32	0.750	0.470	0.320	0.430	0.320
Total	99.570	99.400	99.450	99.980	101.670	98.810	99.45	99.860	99.290	99.470	98.9	98.72	100.160	99.710	99.570	100.150	99.720
											2.418	2.457					
Si	2.660	2.622	2.658	2.660	2.749	2.437	2.658	2.670	2.693	2.529	0.001	0.002	2.642	2.497	2.480	2.514	2.474
Ti	0.000	0.000	0.001	0.002	0.001	0.001	0.001	0.000	0.000	0.002	1.541	1.515	0.000	0.000	0.001	0.001	0.001
$Al^{3}+$	1.320	1.368	1.337	1.317	1.236	1.534	1.337	1.312	1.287	1.435	0	0	1.357	1.466	1.493	1.460	1.490
$Fe^{3}+$	0.011	0.006	0.000	0.013	0.012	0.020	0	0.009	0.011	0.027	0.027	0.016	0.009	0.025	0.016	0.018	0.018
$Mg^{2}+$	0.000	0.001	0.000	0.009	0.010	0.005	0	0.001	0.001	0.002	0.004	0.003	0.001	0.001	0.001	0.002	0.001
$Ca^{2}+$	0.354	0.396	0.352	0.369	0.283	0.567	0.352	0.391	0.322	0.487	0.592	0.555	0.369	0.508	0.525	0.490	0.536
Na	0.612	0.565	0.607	0.568	0.615	0.423	0.607	0.547	0.638	0.490	0.41	0.435	0.549	0.491	0.479	0.500	0.480
K	0.045	0.032	0.041	0.039	0.056	0.018	0.041	0.027	0.049	0.025	0.019	0.019	0.043	0.027	0.018	0.025	0.018
Sum	5.003	4.989	4.997	4.977	4.962	5.005	4.997	4.956	5.001	4.996	5.012	5.002	4.971	5.017	5.013	5.009	5.019
Ab	60.491	56.908	60.714	58.190	64.452	41.948	60.714	56.691	63.180	48.881	40.168	43.086	57.110	47.838	46.866	49.273	46.397
An	35.021	39.908	35.218	37.801	29.681	56.230	35.218	40.539	31.921	48.602	57.926	55.065	38.434	49.508	51.328	48.280	51.826
Or	4.488	3.183	4.068	4.010	5.867	1.822	4.068	2.770	4.899	2.517	1.906	1.849	4.456	2.655	1.806	2.447	1.777

PH-C= phenocryst-core; **PH-R=** phenocryst rim; **MP=** microphenocryst; **MIC=** microlite.

Cations recalculated on the basis of 8 oxygens.

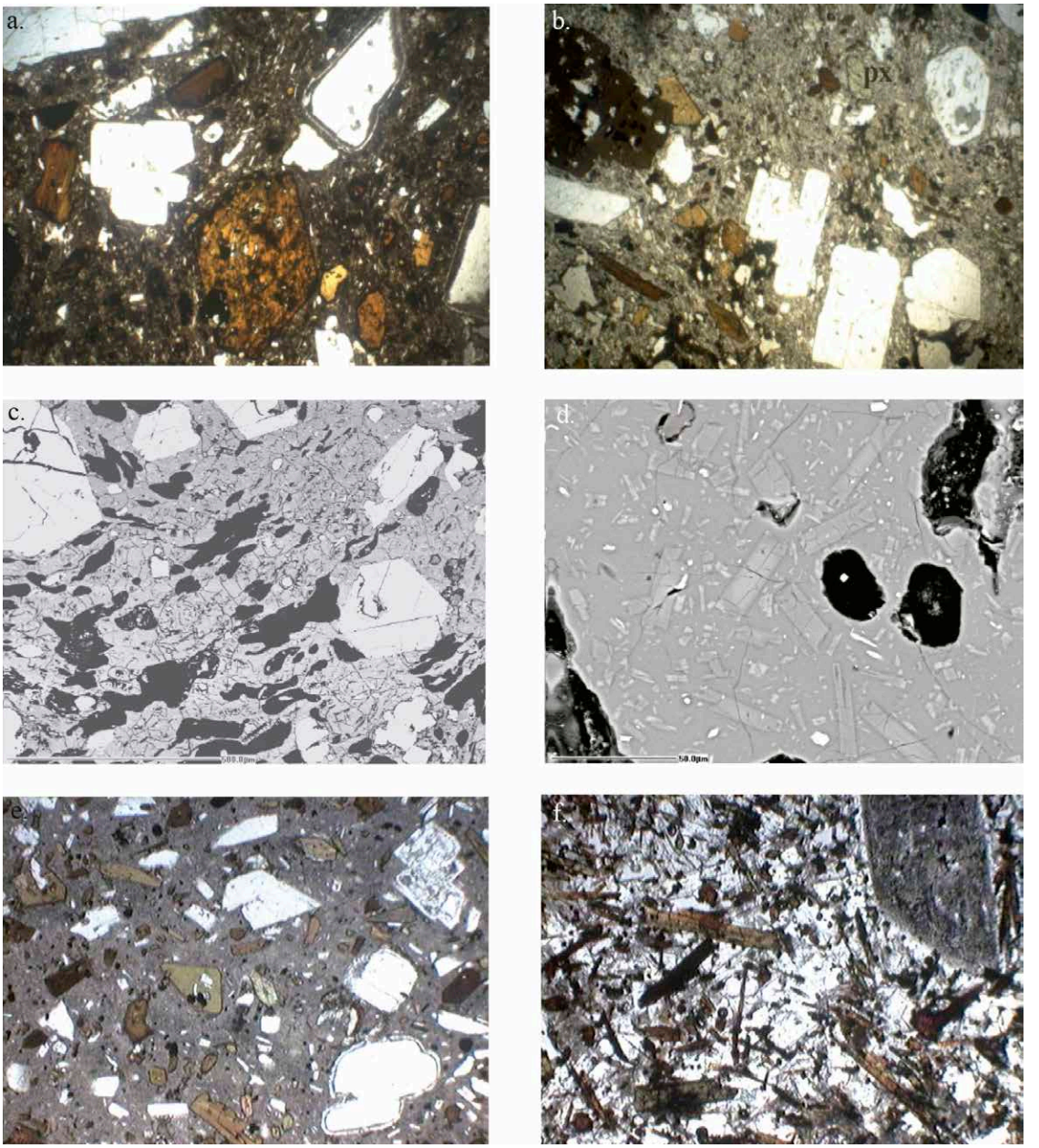

FIG. 10. Photomicrographs (in plane-polarised light) of Domo Tinto samples. **a.** TD08-sample from the massive interior of a lobe highlighting seriate-textured plagioclase and pseudomorphed character common to amphibole crystals; **b.** TD10-sample from the outer surface of a summit hummock. This sample exhibits a vesicular nature (irregular dark patches) and a population of fresh amphiboles, a rare feature in the Domo Tinto sample suite. Also note the rare pyroxene crystal (px); **c.** TD10-Backscattered SEM image of a summit hummock sample showing the vesicular nature of this lava, only seen in the upper zones of hummocks. Black areas represent the elongate squashed vesicles prevalent in this sample. Note the scale bar; **d.** TD08-SEM photomicrograph of the groundmass texture of the Tinto lava. An apparent feature is the presence of two size populations of plagioclase microlites. The light-grey interstitial material is the groundmass composed predominantly of devitrification crystals of quartz and K-feldspar and minor glassy patches. Note the scale bar; **e.** TD14-sample of Northern Summit lava, highlighting the distinctly different population of fresh, microphenocrystic amphiboles not seen in the dome-lava; **f.** TD01-photomicrograph of mafic inclusion from Domo Tinto highlighting the dictytaxitic texture of this sample. Note the spongy plagioclase xenocryst (upper right) with well-developed reaction rim.

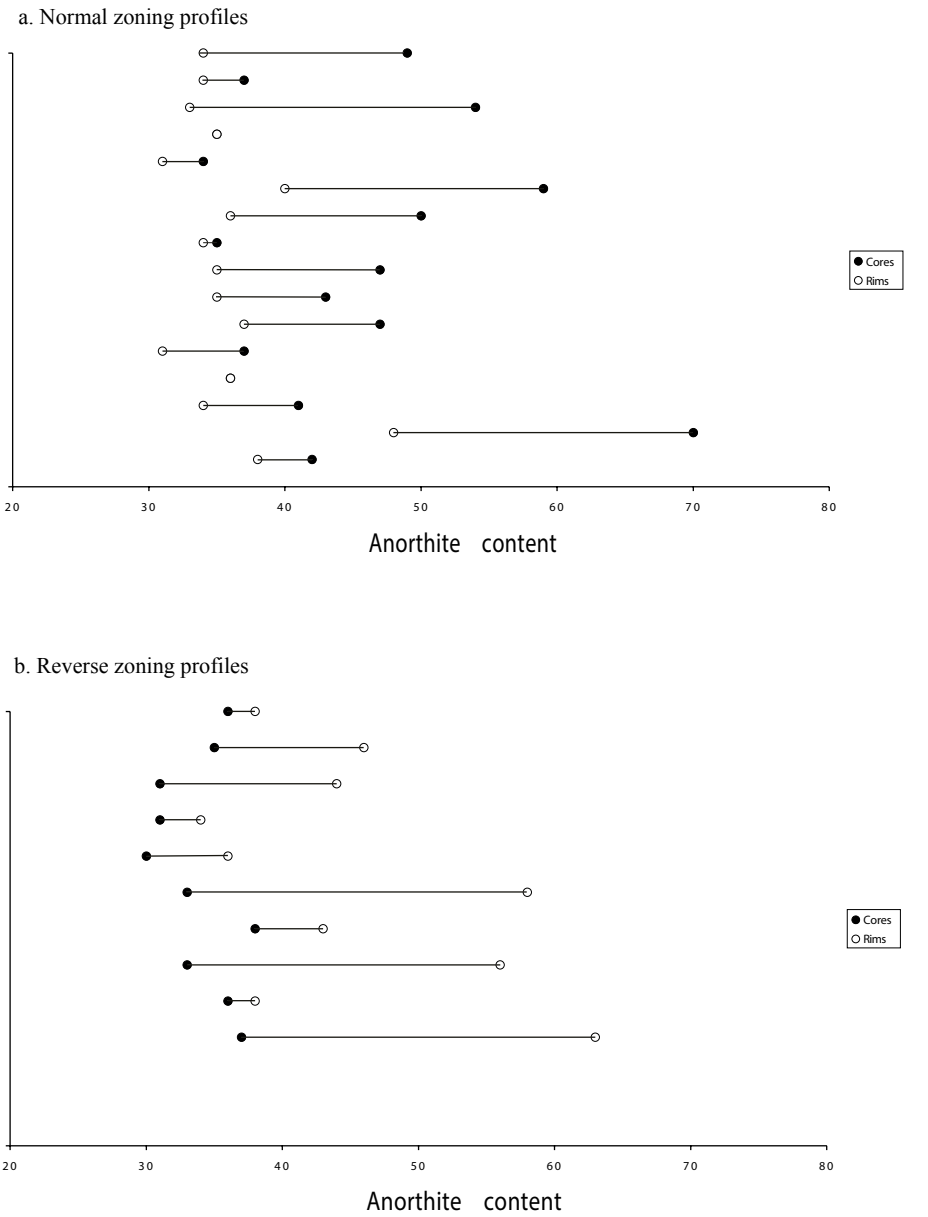

FIG. 11. **a.** Graph showing examples of normally zoned plagioclase phenocrysts highlighting the change in anorthite content from core to rim; **b.** Similar graph showing examples of reversely zoned phenocrysts in the Domo Tinto lavas.

are re-crystallised to form opaque Type 3 examples. There are inclusions of plagioclase (~An_{35}) and euhedral Fe-Ti oxides. One sample (#TD10) from the summit contains fresh amphibole phenocrysts (Fig. 10b) and fresh amphibole microlites (both edenite and magnesiohastingsite) also occur in the groundmass. A feature also unique to this sample is the presence of clusters of interlocking micro-phenocrysts of fresh amphibole and plagioclase. Twinning is rare and occasional phenocrysts with reacted cores were seen. This sample (#TD10) from the upper surface of a summit hummock exhibits several significant features unique to the dome and these include its enhanced vesicularity, higher microlite content, an unaltered amphibole population and the microphenocrystic clusters.

TABLE 3. REPRESENTATIVE MICROPROBE ANALYSES OF AMPHIBOLE CRYSTALS WITHIN THE TINTO LAVAS (TD) AND THE MAFIC INCLUSIONS (MI).

Sample	TD	TD	TD	TD	TD	TD	TD	TD	TD	MI	MI	MI	MI	MI	MI	MI
	TD10	TD10	TD10	TD08	TD10	TD10	TD08	TD08	TD10	TD01	TD01	TD01	TD01	TD01	TD01	TD01
Type	Ph-C	Ph-C	Ph	MP	MP	MP	MIC	MIC	MIC	PH-C	PH-C	MP	MP	MIC	MIC	MIC
SiO_2	45.020	45.720	41.630	41.160	41.950	44.920	46.030	41.230	41.440	47.450	46.410	40.940	41.950	41.230	39.830	40.690
TiO_2	2.020	1.870	3.500	2.450	3.210	2.140	1.770	3.400	3.270	2.640	1.830	3.290	3.350	3.490	3.350	3.400
Al_2O_3	8.680	7.450	12.060	10.740	11.080	8.910	7.330	11.750	11.170	11.470	7.400	11.950	11.200	11.150	12.550	11.840
Cr_2O_3	0.000	0.110	0.000	0.010	0.000	0.000	0.060	0.000	0.000	0.090	0.000	0.040	0.000	0.010	0.000	0.030
Fe_2O_3	4.610	4.120	4.260	3.030	5.310	6.140	3.550	5.440	5.550	0.000	3.720	5.520	4.300	5.710	4.350	7.930
FeO	10.240	9.900	7.280	12.650	7.150	7.440	9.500	6.040	6.960	12.730	10.310	7.280	6.000	6.440	9.530	4.520
MnO	0.340	0.250	0.150	0.280	0.110	0.280	0.410	0.130	0.200	0.320	0.000	0.170	0.000	0.100	0.070	0.100
MgO	13.280	14.030	13.970	11.640	13.800	13.900	14.030	14.330	13.730	9.660	14.030	13.310	15.040	14.450	12.590	14.510
CaO	11.650	11.880	11.480	11.730	11.180	11.160	11.580	11.490	11.490	8.830	11.830	11.250	11.360	11.640	11.890	11.250
Na_2O	1.960	1.810	2.500	2.640	2.460	1.810	1.760	2.290	2.210	2.140	1.730	2.450	2.670	2.510	2.570	2.530
K_2O	0.940	0.760	0.850	1.010	0.760	0.830	0.770	0.920	0.670	1.650	0.690	0.820	0.810	0.720	0.760	0.780
H_2O(c)	2.050	2.040	2.050	1.990	2.030	2.050	2.030	2.040	2.020	2.050	2.050	2.020	2.040	2.040	2.010	2.050
TOTAL	100.790	99.940	99.740	99.310	99.060	99.570	98.820	99.050	98.710	99.020	100.010	99.040	98.720	99.490	99.480	99.630
Si	6.584	6.716	6.100	6.214	6.192	6.574	6.805	6.075	6.143	6.944	6.791	6.066	6.173	6.068	5.937	5.964
Ti	0.223	0.206	0.386	0.278	0.357	0.235	0.197	0.377	0.365	0.290	0.201	0.367	0.371	0.387	0.375	0.375
Al/Al IV	1.416	1.284	1.900	1.786	1.808	1.426	1.195	1.925	1.857	1.056	1.209	1.934	1.827	1.932	2.063	2.036
Al VI	0.081	0.006	0.183	0.126	0.120	0.111	0.083	0.114	0.094	0.923	0.068	0.151	0.116	0.003	0.142	0.009
Cr	0.000	0.013	0.000	0.001	0.000	0.000	0.007	0.000	0.000	0.010	0.000	0.005	0.000	0.001	0.000	0.003
Fe^{3+}	0.507	0.456	0.469	0.344	0.590	0.676	0.394	0.603	0.619	0.000	0.410	0.616	0.477	0.632	0.488	0.875
Fe^{2+}	1.252	1.216	0.892	1.597	0.883	0.911	1.175	0.745	0.862	1.558	1.262	0.902	0.739	0.793	1.188	0.554
Mn^{2+}	0.042	0.031	0.019	0.035	0.014	0.034	0.051	0.016	0.025	0.040	0.000	0.021	0.000	0.013	0.009	0.012
Mg	2.895	3.072	3.051	2.620	3.036	3.033	3.092	3.146	3.035	2.108	3.059	2.939	3.298	3.171	2.797	3.171
Ca	1.826	1.870	1.803	1.897	1.769	1.751	1.834	1.814	1.825	1.385	1.855	1.785	1.791	1.836	1.899	1.767
Na	0.556	0.516	0.711	0.772	0.704	0.512	0.504	0.655	0.637	0.607	0.490	0.704	0.760	0.715	0.741	0.719
K	0.175	0.142	0.159	0.194	0.143	0.155	0.145	0.172	0.127	0.308	0.129	0.156	0.151	0.134	0.144	0.146
OH	2	2	2	2	2	2	2	2	2	2	2	2	2	2	2	2
Sum of Cations	17.557	17.528	17.673	17.863	17.616	17.418	17.483	17.641	17.589	17.228	17.474	17.644	17.703	17.686	17.784	17.631
XMg	0.698	0.716	0.774	0.621	0.775	0.769	0.725	0.809	0.779	0.575	0.708	0.765	0.817	0.800	0.702	0.851

PH-C= phenocryst cores; **MP**= microphenocryst; **MIC**= microlite.

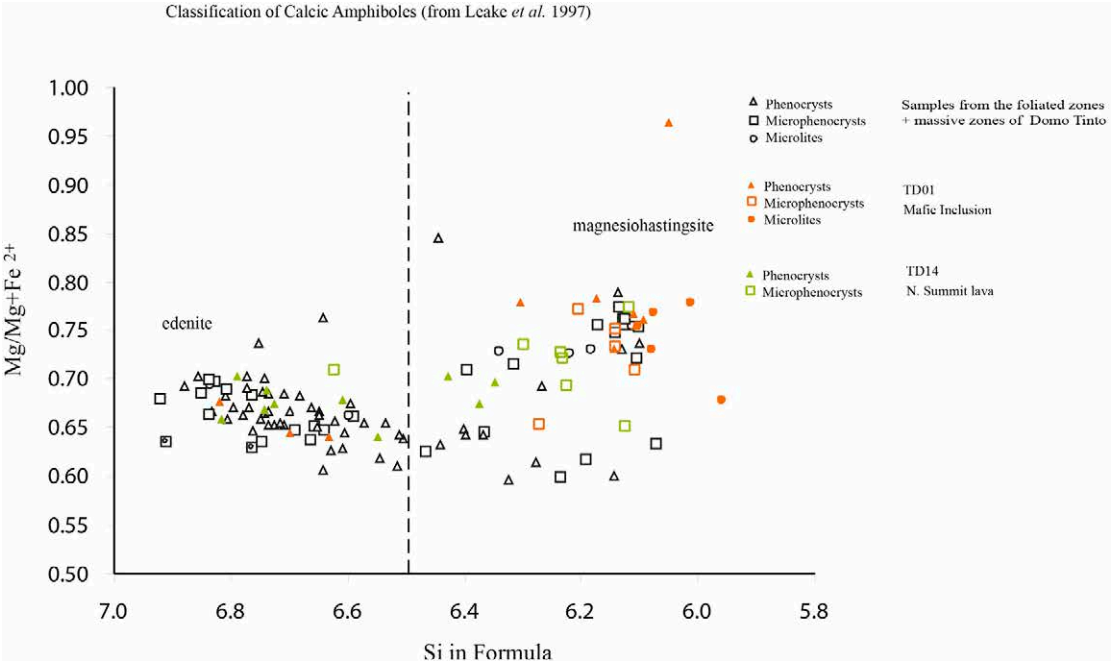

FIG. 12. Mineralogy of the calcic amphibole crystals analysed from the Domo Tinto host lavas and the mafic inclusions found within the host.

The only other common phenocryst phase is biotite mica (Tables 1 and 4). Biotite occurs as relatively large, euhedral crystals (up to 5 mm diameter) that contain ubiquitous inclusions of Fe-Ti oxides and plagioclase. Biotite phenocrysts (~2 vol.%), always exhibit a thick reaction rim with corroded crystal edges (Fig. 10b). Most examples contain plagioclase (~An_{47} core) and Fe-Ti oxide inclusions.

Rare anhedral microphenocrysts of augite (Fig. 10b) were identified (Table 4). These crystals have extremely embayed crystal faces and contain many inclusions of plagioclase and Fe-Ti oxide minerals. Fe-Ti oxide microphenocrysts and microlites are also ubiquitous in the groundmass (~2 vol.%) predominantly as the titano-magnetite variety and rare ilmenite. The only other accessory mineral observed in the Tinto lava was apatite, which was only present as euhedral inclusions within feldspar phenocrysts.

The most significant differences between the Domo Tinto lava samples are found in the nature of their groundmass texture. The thin, foliated zones (up to 65 cm total thickness) are composed of thin, parallel layers (between 1-3 cm thick) of dark-grey coloured layers and more vesicular, dull-orange layers. There are no sharp boundaries between both these textural types and the differences are only subtle under the microscope. The orange layers are notably more vesicle-rich and appear more friable than the dark grey layers which have a glassier appearance. The crystal content between both types is similar suggesting that the variations in vesicle content produce the colour variations. The colour difference is most easily explained as variations in the degree of oxidation caused by fluids percolating through the more vesicular and hence more permeable zones. In this way, the orange layers are notable for their vesicularity which invokes the colour change. The plagioclase microlites (~40 vol.% of groundmass) show a random orientation yet also exhibit a flow foliation akin to the crudely-aligned phenocrysts (Fig. 10a). The groundmass contains two very different crystalline textures. Part of the groundmass consists of elongate feldspar microlites. The material in between the microlites consists of very fine-grained birefringent material which is composed of quartzo-feldspathic material. Crystals can only be resolved under the highest power and this material is interpreted as devitrification with only very small patches of fresh glass preserved. Despite the rocks having a glassy appearance there is, in fact, little remnant glass.

TABLE 4. TABLE OF REPRESENTATIVE MICROPROBE ANALYSES OF BIOTITE AND RARE PYROXENE CRYSTALS IN THE DOMO TINTO LAVAS (TD) AND MAFIC INCLUSIONS (MI).

	BIOTITE														PYROXENE			
Sample	TD TD08	TD TD10	TD TD10	TD TD10	TD TD05	TD TD05	TD TD08	TD TD08	TD TD04	TD TD04	TD TD04	TD TD04	MI TD01	MI TD01	Point	TD TD08	TD TD05	TD TD08
Type	PH-C	PH-C	PH-C	PH-C	PH-C	PH-C	PH-C	PH-C	PH-C	PH-C	PH-C	PH-C	PH-C	PH-C	Label	PH-C	PH-C	PH-C
SiO_2	36.410	37.050	36.220	36.480	36.160	36.570	36.530	37.090	35.550	36.500	36.580	36.490	36.440	36.410	SiO_2	51.740	52.950	51.740
TiO_2	4.890	5.130	5.210	5.000	5.000	5.150	4.940	5.320	4.910	4.980	4.880	5.250	5.270	4.890	TiO_2	0.180	0.170	0.180
Al_2O_3	13.400	13.630	13.520	13.150	13.240	13.320	13.190	13.670	13.190	13.250	13.310	13.370	13.490	13.400	Al_2O_3	1.150	1.010	1.150
Cr_2O_3	0.000	0.000	0.090	0.000	0.000	0.010	0.040	0.000	0.000	0.000	0.000	0.030	0.000	0.000	Cr_2O_3	0.000	0.050	0.000
FeO	15.480	15.850	16.380	15.710	15.700	15.860	15.710	15.010	18.450	15.740	16.170	15.680	16.530	15.480	$Fe_2O^3(c)$	2.320	2.150	2.320
MnO	0.170	0.110	0.200	0.140	0.240	0.130	0.110	0.000	0.000	0.000	0.000	0.270	0.000	0.170	FeO(c)	7.260	6.830	7.260
MgO	13.820	14.680	13.880	14.190	13.850	14.190	13.930	15.020	12.060	14.030	13.980	13.640	13.790	13.820	MnO	0.000	0.560	0.000
CaO	0.010	0.000	0.000	0.030	0.010	0.000	0.000	0.050	0.000	0.000	0.000	0.000	0.010	0.010	MgO	13.270	14.000	13.270
Na_2O	0.660	0.700	0.660	0.940	0.630	0.630	0.580	0.730	0.550	0.620	0.620	0.570	0.640	0.660	CaO	22.550	22.630	22.550
K_2O	8.600	8.720	8.580	8.600	8.830	8.580	8.640	8.990	8.740	8.720	8.920	8.350	9.120	8.600	Na_2O	0.470	0.450	0.470
$H_2O(c)$	3.920	4.020	3.950	3.940	3.910	3.950	3.920	4.030	3.850	3.930	3.940	3.930	3.970	3.920	K_2O	0.010	0.010	0.010
TOTAL	97.350	99.890	98.710	98.170	97.580	98.390	97.590	99.920	97.300	97.750	98.400	97.570	99.260	97.350	TOTAL	98.960	100.820	98.960
Si	5.576	5.530	5.497	5.553	5.545	5.546	5.584	5.521	5.535	5.571	5.563	5.571	5.511	5.576	Si	1.954	1.959	1.954
Ti	0.563	0.576	0.595	0.572	0.576	0.587	0.568	0.596	0.575	0.571	0.559	0.603	0.599	0.563	Ti	0.005	0.005	0.005
Al/Al IV	2.418	2.398	2.418	2.359	2.392	2.382	2.377	2.399	2.419	2.383	2.385	2.406	2.404	2.418	Al/Al IV	0.046	0.041	0.046
Al VI	0.000	0.000	0.000	0.000	0.000	0.000	0.000	0.000	0.000	0.000	0.000	0.000	0.000	0.000	Al VI	0.005	0.003	0.005
Cr	0.000	0.000	0.010	0.000	0.000	0.001	0.004	0.000	0.000	0.000	0.000	0.004	0.000	0.000	Cr	0.000	0.001	0.000
$Fe^{2}+$	1.982	1.979	2.079	1.999	2.014	2.012	2.008	1.868	2.402	2.009	2.056	2.002	2.091	1.982	$Fe^{3}+$	0.066	0.060	0.066
$Mn^{2}+$	0.022	0.014	0.026	0.018	0.032	0.017	0.014	0.000	0.000	0.000	0.000	0.035	0.000	0.022	$Fe^{2}+$	0.229	0.211	0.229
Mg	3.153	3.265	3.140	3.218	3.165	3.209	3.174	3.333	2.799	3.192	3.168	3.104	3.108	3.153	$Mn^{2}+$	0.000	0.018	0.000
Ca	0.001	0.000	0.001	0.005	0.002	0.000	0.000	0.008	0.000	0.000	0.000	0.000	0.002	0.001	Mg	0.747	0.772	0.747
Na	0.196	0.204	0.194	0.277	0.186	0.184	0.171	0.211	0.165	0.183	0.183	0.169	0.188	0.196	Ca	0.912	0.897	0.912
K	1.680	1.660	1.661	1.670	1.727	1.660	1.685	1.707	1.736	1.697	1.730	1.626	1.758	1.680	Na	0.035	0.032	0.035
OH	4	4	4	4	4	4	4	4	4	4	4	4	4	4	Sum of Cations	4	4	4
Sum of Cations	19.591	19.627	19.621	19.670	19.639	19.597	19.585	19.643	19.631	19.607	19.643	19.519	19.661	19.591				
XMg	0.614	0.623	0.602	0.617	0.611	0.615	0.612	0.641	0.538	0.614	0.606	0.608	0.598	0.614	Wo(Ca)	48.310	47.697	48.310
															En(Mg)	39.557	41.064	39.557
															Fs($Fe^{2}+$)	12.133	11.239	12.133

PH-C= phenocryst core.

Thin massive layers intercalated with the foliated zones (up to 1 m thick) in hand specimen appear to be a hybrid of both types of layers seen in the foliated zone in hand specimen. A mottled grey-orange colour is produced by irregular patches of dark grey glass and more vesicular groundmass of orange colour. Both the vesicles and glassy patches appear to be randomly distributed and phenocrysts exhibit a random orientation (Fig. 10b). Devitrification features are a significant component of the groundmass with only very small patches of fresh glass observed.

The main zones of massive lava notably exhibit a consistent light-grey colour with no glassy patches in evidence. The fresh appearance of these thick zones of massive lava probably results from the complete absence of fluid filtration affecting and thus oxidising the groundmass in these parts of the dome. Phenocrysts are randomly oriented within a moderately vesicular glass containing ~40 vol.% microlites (Fig. 10a). Again, the groundmass glass is predominantly altered to a mosaic of devitrification products of microcrystalline equi-granular quartz and feldspar.

The summit hummock lava (#TD10) is light-grey lava and has the most vesicular character on the dome giving it a relatively friable nature. The groundmass contains a moderate amount of flow-aligned plagioclase microlites (~25 vol.%) sitting within a glass marked by well-developed equi-granular devitrification crystals (Fig. 10c). Another feature, seemingly unique to this part of the lava, is the relatively low phenocryst content (~29 vol.%) although this is attributed to the high vesicle content of this sample (Table 1).

The groundmass is pervasively devitrified (Fig. 10d) preventing accurate determination of its composition which consists of stubby micron-size crystallites of quartz, K-feldspar and plagioclase (determined qualitatively using scanning electron microscopy) with extremely small interstitial patches of glass (~1 to 2 μm dia.).

4.3. Northern Summit Lava

Sample #TD14 was collected from a meter-sized block sitting within a glacial moraine deposit covering the northern summit of the dome. It has a relatively high crystal content at ~47 vol.% (Table 1) sitting in a fresh groundmass although the constituent minerals are the same as the lava forming Domo Tinto (Fig. 10e). Seriate-textured plagioclase predominates (~27 vol.%) with subhedral/anhedral habit with many phenocrysts having reaction rims or extremely corroded edges. Plagioclase compositions cover a wide range (An_{28}-An_{61}) and crystals with reaction rims are commonly normally-zoned (Fig. 10e). A few sieve-textured crystals are also present.

Amphibole is very abundant (~16 vol.%), generally with a fresh appearance and only thin reaction rims (Table 1). This phase is particularly common as microphenocrysts exhibiting a prismatic form (Fig. 10e). Compositions of the phenocrystic amphiboles generally plot in the edenite field (with some magnesiohastingsite examples) whilst microphenocrysts are predominantly of the magnesiohastingsite variety (Fig. 12). Occasional phenocrysts of biotite mica are also present containing many plagioclase and Fe-Ti oxide inclusions. Biotite has a euhedral habit and is commonly associated with prismatic amphiboles. Amphibole microphenocrysts are also seen in clusters with plagioclase and Fe-Ti oxides and these are believed to be fragments plucked away from a cumulate zone. Some large amphibole phenocrysts (~5 mm) have been reacted intensely and exhibit thin reaction rims with many plagioclase inclusions. Anhedral clinopyroxene (~1 vol.%) with characteristic inclined extinction and weak pleochroism is also present. Subhedral microphenocrysts and microlites of opaque minerals (~3 vol.%) are also ubiquitous to this sample. All the component crystals sit randomly within a slightly devitrified, microlite-poor glass (Fig. 10e). The overall nature and geochemistry of this block would suggest that it is glacial debris carried down from a higher part of Guallatiri Volcano therefore it is not directly related to the Domo Tinto magma body.

4.4. Mafic Inclusions

The lava of Domo Tinto contains conspicuous, ovoid mafic inclusions (~0.5 vol.%), up to 20 cm in diameter (Fig. 13), a feature that is very common in Pleistocene-Holocene andesitic and dacitic lavas of the Central Andes (*e.g.,* the Chao Dacite; de Silva *et al.*, 1994). An inclusion sample (#TD01) displays a dictytaxitic texture (Fig. 10f) and a fine-grained boundary with the host lava, both characteristic of quenching during a magma-mingling event (Bacon, 1986; Mortazavi and Sparks, 2004). This rock contains a limited mineralogy of plagioclase, amphibole and Fe-Ti oxide with rare biotite xenocrysts.

FIG. 13. Photograph of an ovoid basaltic andesite inclusion mingled within the Tinto lava on a hummock near the dome summit.

Plagioclase (~63 vol.%) is bimodal with one small population (~5 vol.%) of prominent sub-rounded phenocrysts exhibiting reaction rims and sieve textures (Fig. 9). These phenocrysts are reversely zoned and span a broad compositional range (An_{37}-An_{65}). These crystals are interpreted as having a xenocrystic origin most likely to have been incorporated into the inclusion from the andesite during the mingling process. The dominant population of plagioclase is as subhedral/anhedral micro-phenocrysts that form an interlocking microcrystalline network with acicular amphiboles (Fig. 10f). The microphenocryst population generally lies within a more restricted compositional range (An_{48}-An_{57}).

Amphiboles are also bimodal, with the predominant type being the fresh, acicular variety (~28 vol.%) that forms part of the main microcrystalline texture. This distinctive habit is characteristic of quench-crystallization, suggesting that they were probably melt at the time of interaction with the andesitic host. Compositionally, the amphiboles cluster within the calcic magnesiohastingsite variety (Fig. 12), however some examples were of the edenite type similar to the andesite suggesting a xenocrystic origin. A subordinate population (~1 vol.%) of subhedral, stubby amphibole microphenocrysts with corroded edges is present. Large phenocrysts of biotite (~2 mm), showing an extremely corroded nature (indicating a xenocrystic origin) are another prominent yet rare feature.

5. Geochemistry of Domo Tinto

All samples have been analysed for major and trace elements by X-ray fluorescence (Table 5). Representative specimens of each sample were crushed and prepared as fused glass beads (for major element analysis) and pressed powder pellets (for trace element analysis) at the University of Bristol Earth Sciences Department whilst analysis was undertaken at Macquarie University, Australia. Analyses were performed on a Spectro X-lab 2000 energy dispersive XRF. A selection of secondary targets are used to produce polarised radiation and secondary self-excitation which is particularly effective for a selected block of elements. The polarisation greatly

TABLE 5. XRF DATA FOR SAMPLES FROM DOMO TINTO. MAJOR ELEMENTS ARE NORMALIZED TO 100 WT% AFTER SUBTRACTING THE LOSS ON IGNITION (LOI).

Sample no.	Tinto Dome Samples		TD01	TD14	TD15	TD17
	MEAN	ST DEV	Mafic Incl.	N. Summit-ML	S. dome-ML	Pumice
SiO_2	61.87	0.29	54.94	65.53	62.40	65.10
TiO_2	1.00	0.03	1.62	0.75	1.00	0.66
Al_2O_3	15.99	0.23	16.54	15.85	16.02	17.33
Fe_2O_3	5.97	0.12	9.09	4.36	5.84	3.96
MnO	0.08	0.00	0.10	0.07	0.08	0.07
MgO	2.57	0.07	4.15	1.79	2.56	1.43
CaO	4.80	0.13	6.50	3.66	4.78	3.41
Na_20	4.16	0.14	3.80	4.24	3.93	4.30
K_20	3.19	0.09	2.69	3.49	3.05	3.50
P_2O_5	0.37	0.03	0.58	0.27	0.35	0.25
LOI*	-	-	0.73	0.62	1.58	2.67
S	258	253	297.2	56.7	1,980	<2.5
Cl	246	121	28.5	491.1	414.1	627.4
V	133	7	226.8	89.4	139.5	63.7
Ni	11	1	21	4.9	11.9	2.3
Rb	91	2	84.1	104	88.8	108.4
Sr	761	15	892.1	681.9	790.2	671.7
Y	12	0.5	15.5	12.8	12.5	12.1
Zr	183	9	204	209.8	181.2	215.3
Nb	11	0.3	11.1	11.4	10.4	11.9
Cs	8	1	10	9.2	9	10.5
Ba	1,090	19	1,003	1,187	1,073	1,299
La	31	2	26.2	33.2	30.1	31.5
Ce	63	3	60.5	65.7	64.7	62.3
Pr	8	2	8.7	5.8	<5.0	5.9
Nd	26	4	31.4	23.7	18.1	18.5
Pb	20	1	14.9	23.1	18.7	26.2
Th	13	0.4	7.1	14.6	12.5	15.8

* LOI is believed to represent H_2O, CO_2 and some sulphur loss.

Trace elements are in ppm. **ML=** Massive Lava.

reduces the scattering background, allowing much shorter count times. The Loss on Ignition (LOI) for each sample was calculated after reweighing each sample following heating in a furnace for 30 minutes at 960°C. The LOI in the results was removed and each analysis was normalized to 100% on an anhydrous basis for further graphical representation of the data. Analyses of International Rock Standards indicate that the accuracy and precision are better than 0.5% absolute for major elements and better than <5% for trace elements.

The Domo Tinto sample suite is typical of a calc-alkaline orogenic series (Table 5). According to the classification of Peccerillo and Taylor (1976) all of the lavas of the dome are high-K andesites apart from the Northern Summit Lava (#TD14) and

the pumice sample from the pyroclastic sequence (#TD17) which are high-K dacites (Fig.14a). The mafic inclusion found within the Guallatiri lava is classified as high-K basaltic andesite. On an AFM diagram, all the rocks of the suite define a classic calc-alkaline trend showing no significant iron-enrichment (Fig. 14b).

The analyses for the sample suite indicate that the andesitic magma was relatively homogeneous prior to eruption of the dome (Table 5). Reviewing this data highlights only minor variations in SiO_2 (61.29-62.21%), MgO (2.49-2.73%), K_2O (3.08-3.35%) and P_2O_5 (0.34-0.42%). This homogeneity is evident in variation diagrams of the major elements K_2O and Al_2O_3 (Figs. 15a and b). The only outliers in the dataset are from #TD01 (a mafic inclusion) #TD14 (the Northern Summit Lava) and #TD17 (a pumice from the pyroclastic sequence). The microphenocryst content and trace element content both indicate that this pumice sample is not related to Domo Tinto and will not be mentioned further. Sample #TD15 was collected from another small dome (here called the South Dome) directly south of the main summit and ~2 km to the northeast of Domo Tinto. Data from this sample usually plot within the Tinto cluster suggesting a genetic link between both domes.

A review of the trace element data, which generally exhibit far greater sensitivity to geochemical changes, reinforce the conclusion that the Tinto magma body was relatively homogeneous. The most significant variations include barium (1,045-1,116 ppm) and strontium (722-784 ppm) and even these are not particularly large. Again, the only outliers to the dataset were the same as those observed in the major element dataset.

6. Magmatic Conditions

A review of the amphibole compositions indicates the presence of two distinct populations demarked by their different Al contents. Simple calculations, on a limited data set, using the geothermobarometer defined by Ridolfi *et al.* (2010) refine our knowledge of the plumbing system beneath Domo Tinto. Our calculations suggest the high-Al amphibole population resided in a relatively deep magma body at 12 to 14 km depth (T=970°C and P=330 MPa) whilst the low-Al amphibole population was in a shallower magma body at 5 to 6 km depth (T=840°C and P=330 MPa). Using the technique of Holland and Blundy (1994) from analyses of co-precipitating amphiboles and plagioclase (either as inclusions in each phase or as adjacent crystals of both phases) alternative estimates for magma temperature were determined. The accuracy of individual temperature calculations are estimated to be 35°-40°C in the range 750 to 1,000°C while the precision is believed to be <15°C (personal communication, J. Blundy, 2002). Although absolute temperatures are not very accurate, the relative differences between mineral assemblages are thought to be real at differences of more than 15°C. For the Tinto andesite magma, an average magmatic temperature of 790°C was determined. Magmatic temperatures of 890°C for the basaltic andesite inclusions were obtained from co-existing amphibole/plagioclase crystals at a distance ~3 cm from the boundary with the andesite lava. Crystal-pairs analyzed within the chilled margin of the basaltic andesite at the boundary of the inclusion produced a range of temperatures between 890°C to 930°C.

7. Discussions

7.1. Evolution of the Domo Tinto magmatic system

Using the petrologic, petrographic and geochemical dataset, observations from this study may be used to constrain the evolution of the andesitic magma body that fed the eruption of Domo Tinto. This magma reservoir was only a small part of the much larger volcanic system beneath Guallatiri Volcano. The most notable feature of the lava is the wide range of disequilibrium textures and the broad range of feldspar compositions, most likely resulting from the mixing of a deeper magma into a shallow magma chamber. The complex zoning patterns of plagioclase phenocrysts and calcic-rich nature of the plagioclase microlites indicate a mush of crystals which have undergone different thermal histories. This can partly be explained by the effects of latent heat release resulting from decompression crystallization (Blundy *et al.*, 2006) as well as compositional mixing through the exchange of crystals and melts (*e.g.,* Bergantz and Breidenthal, 2001). The presence of plagioclase and biotite xenocrysts in the host lava and the mafic inclusions show that pervasive mingling and disaggregation has occurred. Similar petrological features have been described in numerous publications, for example, in the andesite

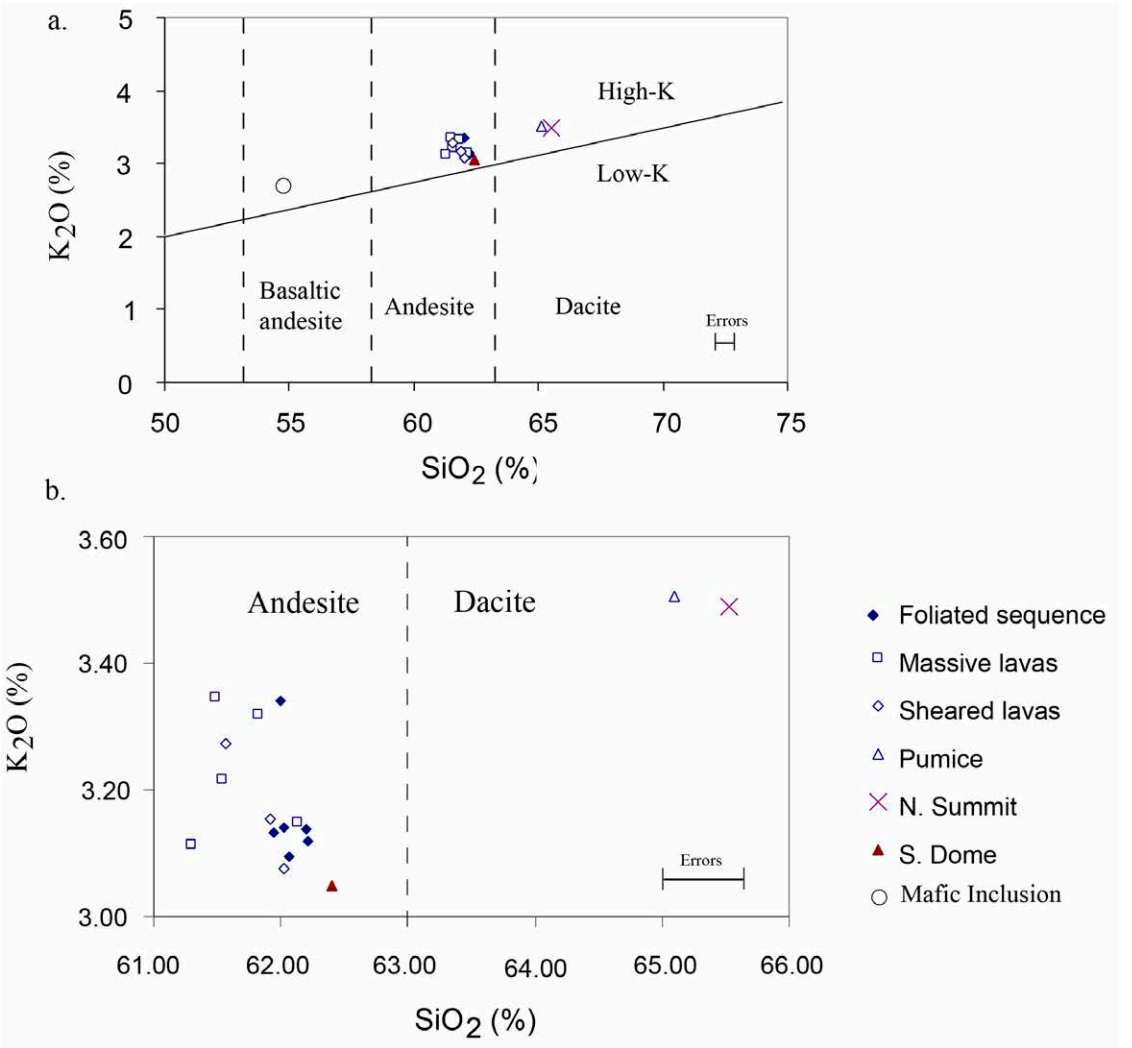

FIG. 14. **a.** Classification of the Domo Tinto sample set using a plot of K_2O against SiO_2 and the compositional fields defined by Peccerillo and Taylor (1976); **b.** Detailed view of the main cluster in **a** of the Tinto lavas. Although there is an apparent trend between the foliated sequence and the massive lavas (possibly suggesting a differentiation effect due to shearing), caution towards any significant meaning to this is needed as all of the data lies close to the error limits of technique.

of the Soufrière Hills Volcano, Montserrat and their development has been ascribed to a process of self-mixing and inclusion disaggregation (Couch *et al.*, 2001; Humphreys *et al*., 2009). In such a scenario, heating by mafic magma at the base of a chamber results in an unstable thermal boundary layer that forms zones of variably heated magma within the chamber. As such, variable compositions between individual crystals within a crystal mush can occur without direct physical involvement of the intruded mafic magma. Similar petrological features have also been detailed at other Central Andean stratovolcanoes (*e.g.,* Ginibre *et al.*, 2002; Ruprecht and Wörner, 2007) suggesting this combination of petrological processes to generate crystal-rich intermediate magmas may be relatively commonplace.

An interesting feature is the presence of amphibole microlites (of edenite and magnesiohastingsite). Groundmass amphiboles were also present in the dacite lava of the 1991-95 Unzen eruption and the implications were studied by Sato *et al.* (1999). A series of melting experiments on the groundmass and

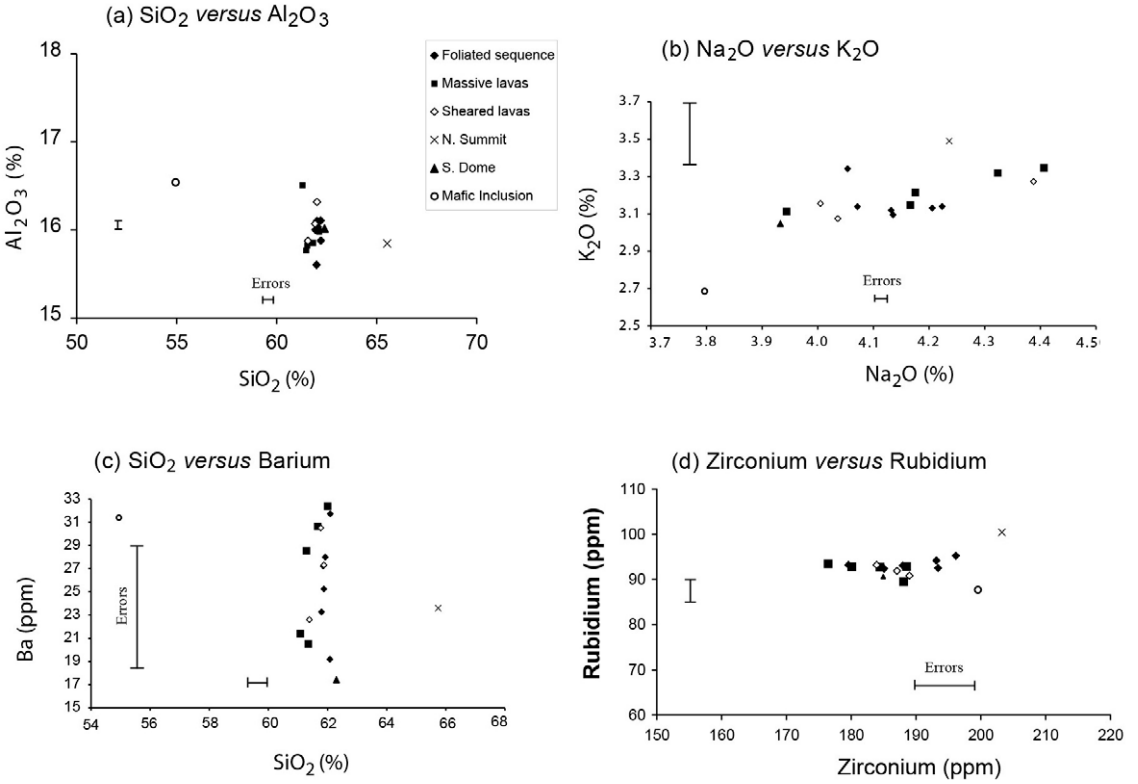

FIG. 15. Variation diagrams of selected major and trace elements highlighting the relative homogeneity of the Domo Tinto magma body-the only clear outliers are from the mafic inclusion (TD01) and the Northern Summit Lava (TD14).

Fe-Ti oxide thermometry determined that crystallization of the pargasitic groundmass occurred within a water-saturated magma at depths >3 km in the conduit (Sato *et al.*, 1999). Comparative chlorine contents between amphibole phenocrysts and microlites also highlighted that both magma mixing and vesiculation/degassing of the magma triggered crystallization of the groundmass amphibole (Sato *et al.*, 1999). If the Tinto magma is considered similar to the Unzen magma, then rapid ascent of the magma occurred at a depth >3 km. In this case, the plagioclase microlites are most akin to the feldspar microphenocrysts of the mafic inclusion (Fig. 9) and must have originated from within the storage chamber rather than as a result of degassing-induced crystallization during slow ascent (Sparks *et al.*, 2000). Similar mixtures of microlite populations have been observed both in the Soufrière Hills andesite and prehistoric silicic eruptions of Mont Pelée, Martinique (Martel *et al.*, 2006). These unusual microlite populations can be formed through incorporation via magma mingling and subsequent inclusion break-up (*e.g.,* Humphreys *et al.*, 2009). The simultaneous growth of both types of plagioclase populations can be explained through a magma-mixing event that may have triggered evacuation of the chamber and rapid ascent prior to emplacement.

Moore and Carmichael (1998) presented water-saturated melting experiments (at pressures up to 3 kbar) on an andesite from Colima volcano in the Western Mexican Volcanic Belt. This andesite (~62% SiO_2) is very similar in whole-rock composition to that of Domo Tinto, except for a higher K_2O content for the Tinto lava. Moore and Carmichael (1998) inferred that the phenocryst content of the andesitic magma could be generated through degassing and re-equilibration on ascent of an initially hydrous parental magma containing >6 wt.% H_2O. In the case of the Tinto lava, with its high modal abundance of amphibole (~10 vol.%) and the presence of biotite phenocrysts (up to 2 vol.%), a similar interpretation is

proposed. However, the complex zoning patterns in the plagioclase crystals and the bimodal amphibole populations suggest a combination of the mixing of two andesitic magmas and simple cooling-related crystallization.

The occurrence of inclusions of basaltic andesite (~0.5 vol.%) indicates magma mixing, commonly considered to be the trigger for an eruption (*e.g.,* Sparks *et al.*, 1977) and this may well be true for Domo Tinto. These inclusions have a distinct dictytaxitic texture implying quench crystallization of a near-complete melt upon interaction with the andesite. The predominance of ovoid mafic inclusions (up to 20 cm long) is indicative that the relative proportion of intruding material is far smaller than that of the host (Sparks and Marshall, 1986) thus true hybridization has not occurred. Petrologic evidence however does show that some degree of physical mixing has taken place. The plot of amphibole compositions clearly shows the two-way contamination of amphibole xenocrysts between the host rock and the inclusions (Fig. 12). Furthermore, the plagioclase phenocrysts contained in the mafic inclusions are all strongly resorbed and reversely zoned suggesting they have been scavenged from the host lava. Extremely altered biotite phenocrysts also within the inclusions are a further clue to a xenocrystic origin.

The petrologic features described indicate that the Tinto eruption was triggered by the intrusion of basaltic andesite melt into the base of a small chamber of crystal-rich andesite. A thermal boundary layer was generated between the two magmas and thermal plumes were developed to induce self-mixing of the resident andesite (Couch *et al.*, 2001). At the interface between the two magmas, the basaltic andesite quenched to crystallize plagioclase and amphibole whilst phenocrysts from the andesite were engulfed into the more-fluid mafic magma. Inclusions of the basaltic andesite were also entrained into the andesite, plucked away from the unstable boundary layer and convectively stirred into the resident crystal mush. During this stage, partial disaggregation of the inclusions occurred leading to contamination of the andesite with plagioclase and amphibole xenocrysts. Repeated invasions of mafic magma into the andesitic host induced physico-chemical interactions until a critical point was breached (*e.g.,* Heiken and Eichelberger, 1980; Clynne, 1999; Annen and Sparks, 2002) and then eruption ensued initiating the formation of Domo Tinto.

7.2. Emplacement of Domo Tinto

Recent observations of dome-forming eruptions, particularly at Soufrière Hills in Montserrat (Watts *et al.*, 2002), Mount Unzen, Japan (Nakada *et al.*, 1999), Mount St. Helens, U.S.A. between 2004 to 2006 (Vallance *et al.*, 2008) and most recently the rhyolitic dome-forming eruption of Volcan Chaitén, Chile (Bernstein *et al.*, 2013) have highlighted the directed extrusion of crystal-rich lava along shear zones and fluctuations in the extrusion rate during the course of an eruption. Here, we review briefly the key aspects of the Soufrière Hills eruption as a framework for interpreting the formation of Domo Tinto.

As a consequence of fluctuating extrusion rates, lava is extruded at varying viscosities with near-solid lava emplaced at low extrusion rates following periods of quiescence. Lava with more fluidal properties that spreads in an axisymmetric manner can be extruded during the more vigorous active stages of a dome eruption. At Soufrière Hills Volcano, in particular there were rare periods when pancake or torta-like lobes extruded. Such domes were composed of small and large angular blocks and commonly developed following a major collapse. Large stubby spines would extrude and rapidly cool and split into smaller, jagged blocks that fell away in all directions (Figure 20 in Watts *et al.*, 2002). This process would repeat itself over several days to form a larger pancake-shaped dome of angular blocks as the fresh blocks pushed away older lava blocks during extrusion. Preservation of these pancake lobes was rare as later growth tended to bulldoze away the loose blocks that formed the pancakes and the lobes evolved into more rugged asymmetric shear lobes. In the case of a period of unsteady eruption rates, following quiescent periods of activity, large viscous plugs were pushed out along shear faults and triggered large-scale dome collapses forming amphitheatre shaped scars with near-vertical sides. Longer periods of more steady growth developed shear lobes with a characteristic clover-leaf shape in plan-view. These structures had a broad, elliptical form with a steep leading edge of massive, jointed lava that developed through alternating exogenous and endogenous inflation into its core (Watts *et al.*, 2002).

The broad-scale features of Domo Tinto, such as its circular shape and moderate aspect ratio suggest a relatively simple, axisymmetric structure. However, the internal features of the dome with internal contacts

suggests a more complex evolution. The foliated zones can be interpreted as shear zones between individual flow lobes with convex, curved surface morphologies. The vesicular lava within the foliated layers most probably was plucked from the upper contact by the overriding lobe. Thus lobe emplacement appears to have involved predominantly exogenous growth of directed structures with a hummocky upper surface that stack up on top of each other (Fig. 16). If the extrusion had been a simple axisymmetric type then features such as concentric compression ridges would be expected on the upper surface. Instead, the presence of lenticular hummocks that trend in a linear pattern radiating away from the centre is evident on Domo Tinto. These lenticular hummocks form a crude, sub-radial pattern indicating localised linear emplacement directions with the hummocks merging down into lenses of massive lava (Fig. 7). These features suggest a model of sequential emplacement in a directed style as depicted in figure 16. Furthermore, both observations at Soufrière Hills volcano and experimental work by Fink and Griffiths (1998) on viscous extrusions highlight axisymmetric structures which preferentially form at rapid discharge rates and are generally composed of large, individual angular blocks. These extrusions do not form zones of massive lava and are easily eroded and removed by later growth episodes. Circular, axisymmetric bodies are more usually observed as a feature of low-viscosity glassy lavas *e.g.,* Little Glass Mountain (Fink 1983). However, the Tinto lava has been described here as one that is moderately rich in both phenocrysts, microphenocrysts and microlites thus of a considerably higher viscosity than glassier examples.

By analogy to the Soufrière Hills eruption, the observations show some similarity to shear lobes that developed during long periods at moderate extrusion rates. Such lobes exhibited a broad, convex-upward structure with a massive, fractured interior and a relatively flat base as described here for Domo Tinto. The foliated lava sequence has not been observed at Soufrière Hills Volcano although close inspection of the basal zones of shear lobes in Montserrat has always been too dangerous to have been attempted but a similar stratigraphy could be envisaged. There are several differences in this comparison though. Such well-preserved lenticular hummocks with sub-radial jointing have not been observed at Soufrière Hills as the upper surfaces have a broader, clover-leaf (or whaleback) shape that fractures in a more irregular fashion. This difference may be a reflection of subtle variations in eruption rate, cooling rate and/or viscosity although the overall manner of directed extrusion of lenticular lobes is still very plausible. Ideally, it would be interesting to highlight any links between the petrologic processes at play and the emplacement of individual lobes of Domo Tinto. However, such relationships are beyond the scope of this study and would be more possible from direct observations and sample collection during the eruptive phase of a lava dome.

The torta-like morphology and small size of Domo Tinto suggests a simpler extrusion history to the Soufrière Hills dome in that the dome never evolved to a situation where dome collapses were triggered. Factors that may have contributed to these differences include:

1. The eruption generally involved a continuous phase of extrusion without any major fluctuations in the extrusion rate. Studies have shown that a major causative factor for dome collapse was the pulse-like activity during dome evolution (Watts *et al.*, 2002).
2. A lower viscosity for the Tinto lava is envisaged favouring more fluid-like behaviour. Despite a similar bulk composition and phenocryst content to the Soufrière Hills lava, there is a marked difference in microphenocryst content (~20 vol.%). The Tinto lava is more clearly bimodal with a higher groundmass/melt content thus petrographic reasoning suggests the Tinto lava is less viscous.
3. A higher extrusion rate with rapid emplacement favouring this behaviour. Magma moves further before crystallization and further degassing. Each lobe shows the characteristics of being thermally immature thereby promoting the emplacement of a smooth-surfaced lobe with no development of blocky lava or breccia at its margins (cf. Naranjo *et al.*, 1992).
4. The slope. Eruption onto a flat surface, such as the bottom of a glacial valley, promoted the radial development of stacked lenticular lobes rather than the formation of a coulée or lava flow feature (*e.g.,* de Silva *et al.*, 1994).
5. A short eruption duration. The small volume of the dome indicates that the system did not have any prolonged history to develop a more complex morphology. For example, an average extrusion rate of 10 m^3/s would have constructed Domo Tinto in only 23 days.

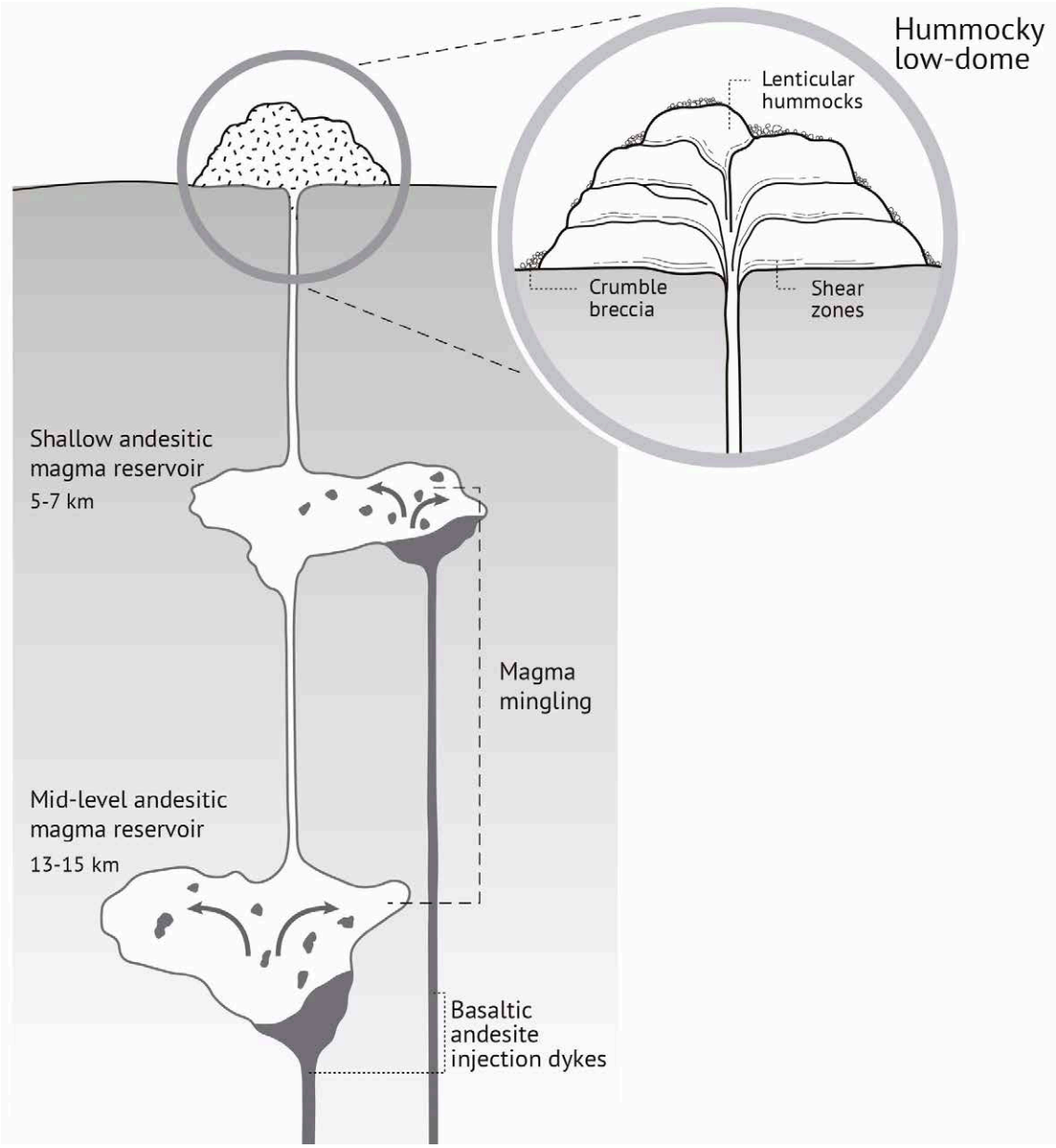

FIG. 16. Schematic cartoon showing the eruption and emplacement of the hummocky low-dome of Domo Tinto following an injection of basaltic andesite into a network of small magma reservoirs that are part of the much larger Guallatiri Volcano magma system.

The features described here for Domo Tinto indicate a relatively benign eruption of viscous lava oozing onto flat topography from a central vent. Development of the dome occurred as distinct lenticular lobes that formed separately through time following minor pulsations in activity with lobes stacking up against or on top of each other. Emplacement of these thermally immature lava lobes probably occurred at fast eruption rates to construct the dome in a relatively short period of time. The overall shape is one that has not been described before and it would be pertinent to introduce a new descriptive dome morphology here termed a 'hummocky low-dome'. Overall, the eruption was a monogenetic extrusion

and this model for its formation may apply to many other small-volume, crystal-rich intermediate domes commonly seen on the flanks of larger edifices.

Acknowledgements

R.B. Watts was funded by a University of Bristol Scholarship, J. Clavero R. by Fondecyt Projects and R.S.J. Sparks received a NERC Fellowship, a Wolfson Royal Society Merit Award and further support from a European Research Council Grant (VOLDIES). Training and supervision was provided by the expertise of R. Brooker (X-Ray Fluorescence) and S. Kearns (Microprobe) in the University of Bristol Earth Sciences Department and is greatly appreciated by R.B. Watts. Particular thanks is extended to G. Anabalón for producing the map figures and to A. Díaz (aka Tuco) and J. Lemp of the Chilean Geological Survey for their driving talents during fieldwork. Insightful reviews by S. de Silva and G. Wörner are greatly appreciated by the authors. Thanks also to S. Couch and C. Bonadonna for their assistance during the field trip of October 1999 and for surviving the driving talents of R.B. Watts particularly around Robertito's Bend somewhere in the Lauca National Park.

References

Annen, C.; Sparks, R.S.J. 2002. Effects of repetitive emplacement of basaltic intrusions on thermal evolution and melt generation in the deep crust. Earth and Planetary Sciences Letters 203: 937-955.

Bacon, C.R. 1986. Magmatic inclusions in silicic and intermediate volcanic rocks. Journal of Geophysical Research 91: 6091-6112.

Bergantz, G.W.; Breidenthal, R.E. 2001. Non-stationary entrainment and tunnelling eruptions: A dynamic link between eruption processes and magma mixing. Geophysical Research Letters 28: 3075-3078.

Bernstein, M.; Pavez, A.; Varley, N.; Whelley, P.; Calder, E.S. 2013. Rhyolitic lava dome growth styles at Chaiten Volcano, Chile (2008-2009): Interpretation of Thermal Imagery. Andean Geology 40 (2): 295-309. doi: 10.5027/andgeoV40n2-a07.

Blake, S. 1990. Viscoplastic models of lava domes. *In* Lava Flows and Domes: Emplacement Mechanisms and Hazard Implications. IAVCEI Proceedings Volcanology, No. 2 (Fink, J.H.,: editor). Springer Verlag: 88-126. Heidelberg.

Blundy, J.; Cashman, K.; Humphreys, M. 2006. Magma heating by decompression-driven crystallization beneath andesite volcanoes. Nature 443: 76-80.

Browne, B.L.; Eichelberger, J.C.; Patino, L.C.; Vogel, T.A.; Uto, K.; Hoshizumi, H. 2006. Generation of porphyritic and equi-granular mafic enclaves during magma recharge events at Unzen Volcano, Japan. Journal of Petrology 47: 301-328.

Bull, K.F.; Anderson, S.W.; Diefenbach, A.K.; Wessels, R.L.; Henton, S.M. 2013. Emplacement of the final lava dome of the 2009 eruption of Redoubt Volcano, Alaska. Journal of Volcanology and Geothermal Research 259: 334-348.

Cashman, K.V.; Thornber, C.R.; Pallister, J.R. 2008. From dome to dust: Shallow crystallization and fragmentation of conduit magma during the 2004-2006 dome extrusion of Mount St. Helens, Washington. *In* A Volcano Rekindled: The First Year of Renewed Eruption at Mount St. Helens 2004-2006 (Sherrod, D.A.; Scott, W.E.; Stauffer, P.H.; editors) US Geological Survey, Professional Paper 1750: 387-413.

Charrier, R.; Hérail, G.; Pinto, L.; García, M.; Riquelme, R.; Farías, M.; Muñoz, N. 2013. Cenozoic tectonic evolution in the Central Andes in northern Chile and west central Bolivia: implications for paleogeographic, magmatic and mountain building evolution. International Journal Earth Sciences 102 (1): 235-264.

Clynne, M.A. 1999. A complex magma mixing origin for rocks erupted in 1915, Lassen Peak, California. Journal of Petrology 40: 105-132.

Couch, S.; Sparks, R.S.J.; Carroll, M.R. 2001. Mineral disequilibrium in lavas explained by convective self-mixing in open magma chambers. Nature 411: 1037-1039.

de Silva, S.L.; Francis, P.W. 1991. Volcanoes of the Central Andes. Springer Verlag: 273 p. Heidelberg.

de Silva, S.L.; Self, S.; Francis, P.W.; Drake, R.E.; Ramírez, C.R. 1994. Effusive silicic volcanism in the Central Andes-The Chao dacite and other young lavas of the Altiplano-Puna Volcanic Complex. Journal of Geophysical Research 99: 17805-17825.

Devine, J.D.; Murphy, M.D.; Rutherford, M.J.; Barclay, J.; Sparks, R.S.J.; Carroll, M.R.; Young, S.R.; Gardner, J.E. 1998. Petrologic evidence for pre-eruptive pressure-temperature conditions, and recent reheating of andesitic magma erupting at the Soufrière Hills Volcano, Montserrat, West Indies. Geophysical Research Letters 25: 3669-3672.

Fink, J.H. 1983. Structure and emplacement of a rhyolitic obsidian flow: Little Glass Mountain, Medecine Lake Highland, northern California. Geological Society of America, Bulletin 94: 362-380.

Fink, J.H.; Griffiths, R.W. 1998. Morphology, eruption rates and rheology of lava domes: Insights from laboratory models. Journal of Geophysical Research 103: 527-545.

García, M.O.; Jacobson, S. 1979. Crystal clots, amphibole fractionation and the evolution of calc-alkaline magmas. Contributions to Mineralogy and Petrology 69: 319-327.

García, M.; Gardeweg, M.; Clavero, J.; Hérail, G. 2004. Hoja Arica, Región de Tarapacá. Servicio Nacional de Geología y Minería, Carta Geológica de Chile, Serie Geología Básica 84: 150 p. 1 mapa escala 1:250.000. Santiago.

Ginibre, C.; Wörner, G.; Kronz, A. 2002. Minor- and trace-element zoning in plagioclase: implications for magma chamber processes at Parinacota Volcano, northern Chile. Contributions to Mineralogy and Petrology 143: 300-315.

González, O. 1995. Volcanes de Chile. Instituto Geográfico Militar: 640 p.

Heiken, G.; Eichelberger, J.C. 1980. Eruption at Chaos Crags, Lasssen Volcanic National Park, California. Journal of Volcanology and Geothermal Research 7: 443-481.

Holland, T.; Blundy, J. 1994. Non-ideal interactions in calcic amphiboles and their bearing on Amphibole-Plagioclase Thermometry. Contributions to Mineralogy and Petrology 116: 433-447.

Hon, K.; Kauhikaua, J.; Denlinger, R.; Mackay, K. 1994. Emplacement and inflation of pahoehoe sheet flows: Observations and measurements of active lava flows on Kileau Volcano, Hawaii. Geological Society of America Bulletin 106: 351-370.

Humphreys, M.; Christopher, T.; Hards, V. 2009. Microlite transfer by disaggregation of mafic inclusions following magma mixing at Soufrière Hills volcano, Montserrat. Contributions to Mineralogy and Petrology 157: 609-624.

Kött, A.; Gaupp, R.; Worner, G. 1995. Miocene to Recent history of the western Altiplano in northern Chile revealed by lacustrine sediments of the Lauca Basin (18°15'-18°40'S/69°30'-69°05'W). Geologische Rundschau 84: 770-780.

Leake, B.E.; Woolley, A.R.; Arps, C.E.S.; Birch, W.D.; Gilbert, M.C.; Grice, J.D.; Hawthorne, F.C.; Kato, A.; Kisch, H.J.; Krivovichev, V.G.; Linthout, K.; Laird, J.; Mandarino, J.A.; Maresch, W.V.; Nickel, E.H.; Rock, N.M.S.; Schumacher, J.C.; Smith, D.C.; Stephenson, N.C.N.; Ungaretti, L.; Whittaker, E.J.W.; Youzhi, G. 1997. Nomenclature of amphiboles: Report of the subcommittee on amphiboles of the International Mineral Association, commission on new minerals and mineral names. American Mineralogist 82: 1019-1037.

Martel, C.; Radadi, Ali, A.; Poussineau, S.; Gourgaud, A.; Pichavant, M. 2006. Basalt-inherited microlites in silicic magmas: evidence from Mount Pelée (Martinique, French West Indies). Geology 34: 905-908.

Moore, G.; Carmichael, I.S.E. 1998. The hydrous phase equilibria (to 3 kbar) of an andesitic and basaltic andesite from western Mexico: constraints on water content and conditions of phenocryst growth. Contributions to Mineralogy and Petrology 130: 304-319.

Montecinos, F. 1963. Observaciones de Geología en el Cuadrángulo de Campanani, Departamento de Arica, Provincia de Tarapacá. Memoria de Título (Unpublished) Universidad de Chile, Departamento de Geología: 109 p.

Mortazavi, M.; Sparks, R.S.J. 2004. Origin of rhyolite and rhyodacite lavas and associated mafic inclusions of Cape Akrotiri, Santorini: the role of wet basalt in generating calc-alkaline silicic magmas. Contributions to Mineralogy and Petrology 146: 397-413.

Muñoz, N.; Charrier, R. 1996. Uplift of the western border of the Altiplano on a west-vergent thrust system, northern Chile. Journal of South American Earth Sciences 9 (3-4): 171-181.

Murphy, M.D.; Sparks, R.S.J.; Barclay, J.; Carroll, M.R.; Brewer, T.S. 2000. Remobilization of andesitic magma by intrusion of mafic magma at the Soufrière Hills Volcano, Montserrat, West Indies. Journal of Petrology 41: 21-42.

Nakada, S.; Shimizu, H.; Ohta, K. 1999. Overview of the 1990-1995 eruption at Unzen: effusion pulsation and groundmass crystallization. Journal of Volcanology and Geothermal Research 89: 1-22.

Naranjo, J.A.; Sparks, R.S.J.; Stasiuk, M.V.; Moreno, H.; Ablay, G.J. 1992. Morphological, structural and textural variations in the 1988-1990 andesite lava of Lonquimay Volcano, Chile. Geological Magazine 129: 657-678.

Newhall, C.G.; Melson, W.G. 1983. Explosive activity associated with the growth of volcanic domes. Journal of Volcanology and Geothermal Research 17: 111-131.

Peccerillo, A.; Taylor, S.R. 1976. Geochemistry of Eocene calc-alkaline volcanic rocks from the Kastamonu area, northern Turkey. Contributions to Mineralogy and Petrology 58: 63-81.

Ridolfi, F.; Renzulli, A.; Puerini, M. 2010. Stability and chemical equilibrium of amphibole in calc-alkaline magmas: an overview, new thermobarometric formu-

lation and application to subduction-related volcanoes. Contributions to Mineralogy and Petrology 160: 45-66.

Ruprecht, P.; Wörner, G. 2007. Variable regimes in magma systems documented in plagioclase zoning patterns: El Misti stratovolcano and Andahua monogenetic cones. Journal of Volcanology and Geothermal Research 165: 142-162.

Sato, H.; Nakada, S.; Fujii, T.; Nakamura, M.; Suzuki-Kamata, K. 1999. Groundmass pargasite in the 1991-1995 dacite of Unzen volcano: phase stability experiments and volcanological implications. Journal of Volcanology and Geothermal Research 89: 197-212.

Simkin, T.; Siebert, L. 1994. Volcanoes of the World, second edition. Smithsonian Institution, Geoscience Press: 349 p. Tucson.

Sparks, R.S.J.; Sigurdsson, H.; Wilson, L. 1977. Magma mixing: a mechanism for triggering acid-explosive eruptions. Nature 267: 315-318.

Sparks, R.S.J.; Marshall, L.A. 1986. Thermal and mechanical constraints on mixing between mafic and silicic magmas. Journal of Volcanology and Geothermal Research 29: 99-124.

Sparks, R.S.J.; Murphy, M.D.; Lejeune, A.M.; Watts, R.B.; Barclay, J.; Young, S.R. 2000. Control on the emplacement of the andesitic lava dome of the Soufrière Hills volcano, Montserrat by degassing-induced crystallization. Terra Nova 12: 14-20.

Sparks, R.S.J.; Young, S.R. 2002. The eruption of Soufrière Hills volcano, Montserrat (1995-1999): overview of scientific results. *In* The eruption of the Soufrière Hills volcano, Montserrat from 1995 to 1999 (Druitt, T.H.; Kokelaar, B.P.; editors). Geological Society of London, Memoirs 21: 45-69.

Swanson, D.; Dzurisin, D.; Holcomb, R.T.; Iwatsubo, E.Y.; Chadwick Jr., W.W.; Casadevall, T.J.; Ewert, J.W.; Heliker, C.C. 1987. Growth of the lava dome at Mount St. Helens, Washington (U.S.A.) 1981-1983. *In* The Emplacement of Silicic Domes and Lava Flows (Fink. J.H.; editor) Geological Society of America, Special Paper 212: 1-16. Boulder.

Vallance, J.W.; Schneider, D.J.; Schilling, S.P. 2008. Growth of the 2004-2006 Lava-Dome Complex at Mount St. Helens, Washington. *In* A Volcano Rekindled: The Renewed Eruption of Mount St. Helens, 2004-2006 (Sherrod, D.A.; Scott, W.E.; Stauffer, P.H.; editors) US Geological Survey Professional Paper 1750: 169-208.

Walker, G.P.L. 1973. Lengths of lava flows. Philosophical Transactions of the Royal Society of London 274: 107-113.

Watts, R.B.; de Silva, S.L.; Jiménez de Ríos, G.; Croudace, I.W. 1999. Effusive eruption of viscous silicic magma triggered and driven by recharge: a case study of the Cerro Chascón-Runtu Jarita Dome Complex in Southwest Bolivia. Bulletin of Volcanology 61: 241-264.

Watts, R.B.; Herd, R.A.; Sparks, R.S.J.; Young, S.R. 2002. Growth patterns and emplacement of the andesitic lava dome at Soufrière Hills Volcano, Montserrat. *In* The Eruption of Soufrière Hills Volcano, Montserrat, from 1995 to 1999 (Druitt, T.H.; Kokelaar, B.P.; editors). Geological Society of London, Memoirs 21: 115-152.

Wörner, G.; Hammerschmidt, K.; Henjes-Kunst, K.; Lezaun, J.; Wilke, H. 2000. Geochronology ($^{40}Ar/^{39}Ar$, K-Ar and He-exposure ages) of Cenozoic magmatic rocks from northern Chile (18º-22ºS): implications for magmatism and tectonic evolution of the Central Andes. Revista Geologica de Chile 27 (2): 205-240. doi: 10.5027/andgeoV27n2-a04.

Manuscript received: February 06, 2014; revised/accepted: August 07, 2014; available online: August 12, 2014.